Recent Progress of Aluminum Base Amorphous Alloys

Recent Progress of Aluminum Base Amorphous Alloys*

Akihisa Inoue, Katsumasa Ohtera+ and Tsuyoshi Masumoto

Institute for Materials Research

(Received December 28, 1989)

Synopsis

During the past three decades, there have been considerable efforts on the production of an amorphous phase in Al base alloy systems and in 1987 the first successful data on the formation of an amorphous alloy with good ductility have been presented in Al-Ni-(Si or Ge) systems. Al base amorphous alloys have been reported to exhibit technologically interesting properties of high fracture strength combined with low density and good corrosion resistance as well as a scientifically important glass transition phenomenon. This review attempts to summarize the fundamental data on the Al base amorphous alloys consisting of metal-metalloid and metal-metal type components and to present the present interpretation on formation, structure and physical properties of the Al-based amorphous alloys.

I. Introduction

Since an amorphous alloy in Au-Si system was produced for the first time by liquid quenching in 1960[1], a great number of amorphous alloys have been developed in the order of noble metal-, transition metal-, refractory metal- and lanthanide metal-based systems. Thus, the amorphization has been achieved in engineeringly important alloy systems containing Fe, Co, Ni, Cu or Ti as a main component and these alloys have practically been used through the utilization of their good mechanical, physical and chemical properties. In addition to the above-described alloy systems, an amorphization of Al-based alloys has actively been tried up to date because of an expectation of obtaining

---

* The 1852th report of Institute for Materials Research.

\+ On leave from Yoshida Kogyo K.K., Yoshida Kurobe 938, Japan.

high strength materials with low density. However, the first successful data of the formation of Al-based amorphous alloys exhibiting good ductility and high strength were presented very recently (in 1987)[2]. This paper is intended to review the recent progress of Al-based amorphous alloys which has mainly been carried out by the present authors.

II. History of Aluminum-based Amorphous Alloys

The formation of Al-based amorphous alloys by liquid quenching was first tried in binary systems of Al-metalloid and Al-transition metal (M) alloys. As a result, it was found in Al-Si[3], Al-Ge[4] and Al-M (M=Cu[5], Ni[6], Cr[7] or Pd[8]) alloys that a coexistent structure of amorphous and crystalline phases is formed only near the holes in their thin foils prepared by the gun quenching technique in which the cooling rate is higher than that for the melt spinning method. However, no amorphous phase without crystallinity was prepared by melt spinning as well as by the gun- and piston-anvil methods. The first formation of an amorphous single phase in Al-based alloys containing more than 50 at% Al was found in 1981 for Al-Fe-B and Al-Co-B ternary alloys[9]. However, these amorphous alloys are extremely brittle and hence have not attracted strong attention. Subsequently, an amorphous phase was found in melt-spun Al-Fe-Si, Al-Fe-Ge and Al-Mn-Si alloys, but they were also very brittle as similar for the Al-(Fe or Co)-B amorphous alloys. It was believed from these data that the brittleness might be an inherent property for Al-based amorphous alloys. In 1987, an amorphous phase with good bending ductility was discovered to be formed at compositions above about 80 at% Al in Al-Ni-Si and Al-Ni-Ge systems[2]. Since the discovery, ductile Al-based amorphous alloys have successively been found in a number of ternary alloys consisting of Al-early transition metal(EM)-late transition metal(LM)[10,11] which are exemplified for Al-Zr-Cu, Al-Zr-Ni and Al-Nb-Ni, followed by Al-lanthanide metal(Ln)-LM ternary alloys[12,13] in which the EM is substituted by Ln, and then Al-Ln binary alloys without M elements[14-16]. The present review on the formation, structure and properties of Al-based amorphous alloys will be described in the order of the metal-metalloid type system of Al-M-(Si or Ge) alloys and the metal-metal type system consisting of Al-EM-LM, Al-Ln and Al-Ln-LM alloys.

III. Metal-Metalloid Amorphous Alloys

1. Formation range of the amorphous alloys[2,17)]

A mostly single amorphous phase defined by no trace of crystallinity in the X-ray diffraction pattern was formed in Al-Si-M (M=Cr, Mo, Mn, Fe, Co or Ni) and Al-Ge-M (M=V, Cr, Mo, Mn, Fe, Co or Ni) systems. No amorphous phase was formed in Al-Si-M systems with M=Ti, Zr, Hf, V, Nb, Ta, W or Cu and Al-Ge-M systems with M=Ti, Zr, Hf, Nb, Ta, W or Cu. Figure 3-1 shows the compositional ranges of Al-Si-M and Al-Ge-M amorphous alloys. Their amorphous phases are formed in the range 12 to 42 at% Si and 8 to 23 %M for Al-Si-M alloys and 12 to 53 %Ge and 8 to 23 %M for Al-Ge-M alloys. The formation range of the Al-Si-M amorphous alloys is the widest for Al-Si-Co, followed by Al-Si-Fe, Al-Si-Mn, Al-Si-Ni and Al-Si-Cr, and that for the Al-Ge-M amorphous alloys is the widest for Al-Ge-Fe and becomes narrower in the order of Al-Ge-Co, Al-Ge-Cr, Al-Ge-V and Al-Ge-Mn. The amorphous phase is also formed in the Al-Si-V system, but it is always coexistent with crystalline phase. Although the compositional ranges of the amorphous phase are almost the same between Al-Si-M and Al-Ge-M systems, one can notice a difference, in that the metalloid concentration ranges are considerably wider for Al-Ge-M than for Al-Si-M and the M concentration range is wider for Al-Si-M.

It is generally known[18)] that the formation of an amorphous alloy is easier in the vicinity of eutectic composition with lower melting temperature. No equilibrium phase diagrams of Al-Si-M and Al-Ge-M alloys are available over the present wide composition ranges. The eutectic composition of Al-Si and Al-Ge binary alloys is 11.3 at% Si and 30.3 at% Ge[19)], being significantly different between both the alloys. The metalloid concentration where the amorphous phase is formed is in the range 12 to 53 %Ge and 12 to 42 %Si. This indicates that the formation range extends over both sides of the eutectic composition of Al-Ge for the Al-Ge-M system and only on the hypereutectic side of Al-

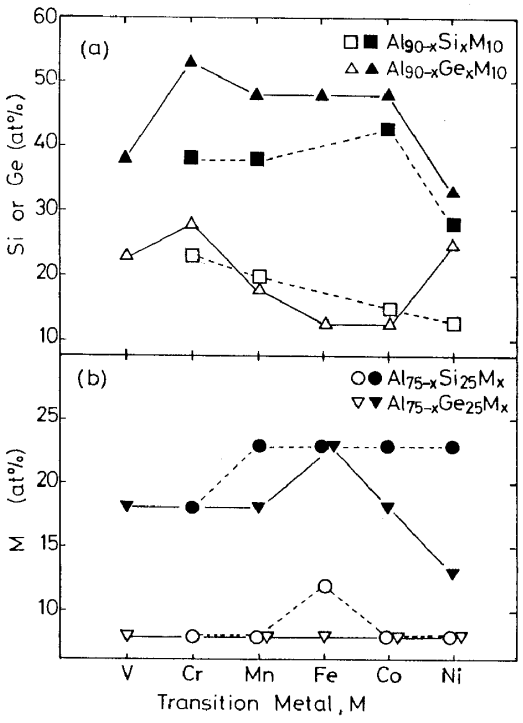

Fig. 3-1 Compositional ranges for the formation of amorphous phase in rapidly quenched $Al_{90-x}(Si\ or\ Ge)_xM_{10}$ (a) and $Al_{75-x}(Si\ or\ Ge)_{25}M_x$ (b) (M=V, Cr, Mn, Fe, Co or Ni) alloys.

Si for the Al-Si-M system. Thus, the lowering of melting temperature (T_m) at a eutectic point is not thought to be a dominant factor for the amorphization of Al-Si-M and Al-Ge-M alloys. On the other hand, the M content for the glass formation is in the range 8 to 23 %, where various kinds of intermetallic compounds are formed in Al-M binary alloys, and T_m is in the range 1533 to 1921 K[19]. The limitation of the M content is probably due to the increase of T_m on the upper side and the decrease of the attractive bonding nature of Al and M atoms for the glass formation on the lower side. In any case, the new information that an amorphous single phase is formed over wide composition ranges in Al-Si-M and Al-Ge-M alloys containing a large amount of Si or Ge without an attractive interaction with Al is different from the general concept[18] for the glass formation of metal-metalloid type alloys. The abnormality is expected to result in the appearance of significantly different structure and properties.

2. Amorphous structure[2,20]

Figure 3-2 shows a bright-field electron micrograph (a) and a selected-area diffraction pattern (b) taken from the electrolytically thinned $Al_{50}Ge_{40}Mn_{10}$ amorphous alloy, along with the X-ray diffraction pattern of the same alloy not subjected to thinning treatment. Lack of contrast characteristic of a crystalline phase in the bright-field image (a) and broad diffuse haloes in the electron and X-ray diffraction patterns (b and c) indicate clearly the formation of an amorphous structure with no trace of crystallinity. The magnitude of the scattering vector defined by $k = 4\pi\sin\theta/\lambda$ at the two peaks of X-ray diffractograms, k_p, was measured to be 23.58 and 31.48 nm^{-1}. From k_p values and the atomic scattering amplitude of each constituent element of Al, Ge and Mn, the two k_p values of the Al-Ge-Mn alloy are analyzed to originate from the Al-Ge interaction for the low-angle halo and Ge-Ge, Al-Mn, and Mn-Mn interactions for the high-angle halo. The two split haloes in the X-ray and electron diffraction patterns were observed for all amorphous alloys in the Al-Si-X and Al-Ge-X (X=V, Cr, Mo, Mn, Fe, Co or Ni) systems.

Figure 3-3 shows a bright-field electron micrograph and a selected-area diffraction pattern of an $Al_{50}Ge_{40}Mn_{10}$ amorphous alloy annealed for 10 min at 520 K with an internal energy lower by about 1.8 kJ/mol as compared with the as-quenched amorphous phase. No change in the contrast revealing the precipitation of a crystalline phase is seen in the bright-field micrograph (a) even after annealing for 10 min at 520 K, while significant changes can be seen in the electron and X-ray diffraction patterns (b) and (c). The changes are summarized as follows:

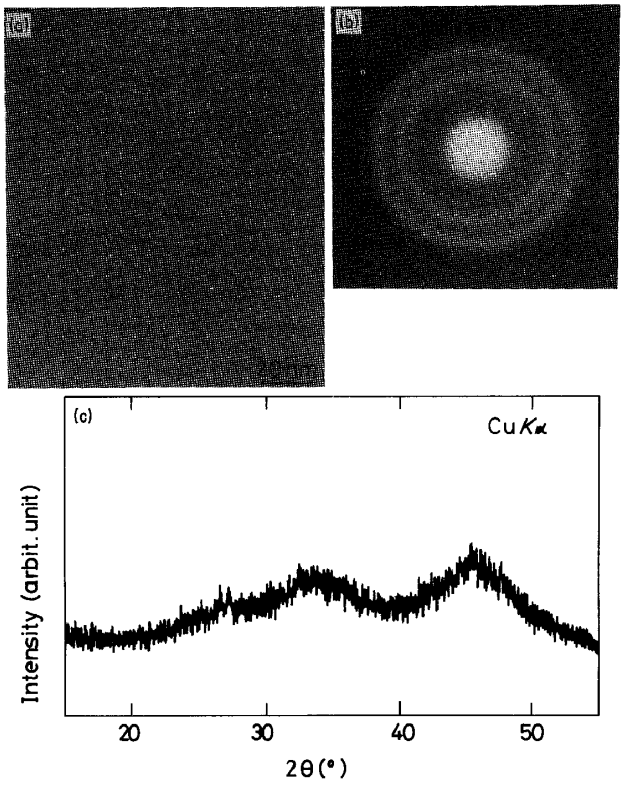

Fig. 3-2 (a) Bright-field electron micrograph, (b) selected-area diffraction pattern and (c) X-ray diffraction pattern of a rapidly quenched $Al_{50}Ge_{40}Mn_{10}$ alloy.

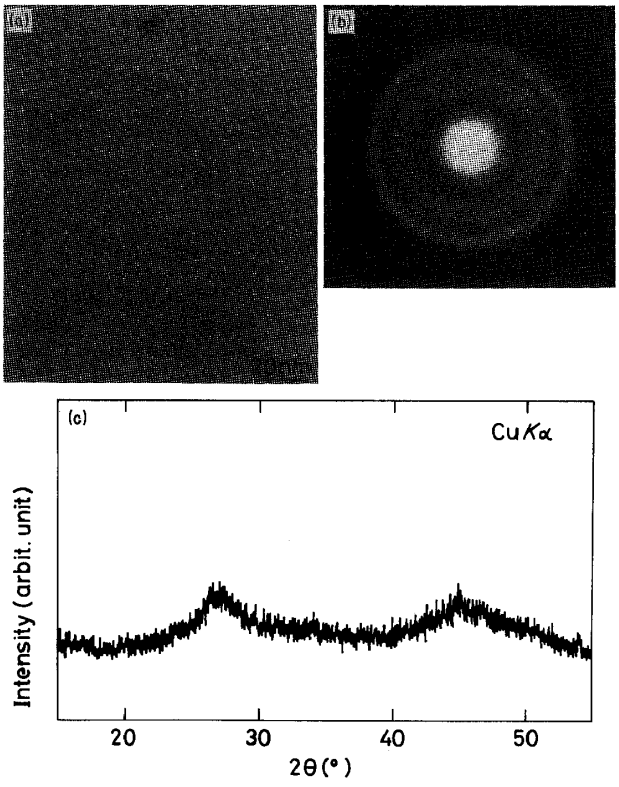

Fig. 3-3 (a) Bright-field electron micrograph, (b) selected-area diffraction pattern and (c) X-ray diffraction pattern of an amorphous $Al_{50}Ge_{40}Mn_{10}$ alloy annealed for 10 min at 520 K.

(1) the broad peak at the low diffraction angle corresponding to k_p=23.58 nm^{-1} decreases significantly and the high-angle diffraction peak at k_p=31.48 nm^{-1} becomes broad; (2) a new broad peak appears at a very low diffraction angle corresponding to k_p=18.77 nm^{-1}.

Considering the significant decrease in the low-angle peak at k_p= 23.58 nm^{-1} resulting from the interaction of Al-Ge atoms, and the broadening of the high-angle peak resulting from the interaction of Ge-Ge and Al-Mn atoms, the structural relaxation upon heating at 520 K for 10 min appears to occur through the decrease in the number of Al-Ge pairs with a weak bonding nature and the increase in the number of Ge-Ge and Al-Mn pairs with a strong bonding nature. The development of the compositional short-range ordering of Ge-Ge pair is also supported from the result obtained from the anomalous X-ray scattering profiles at Ni and Ge K absorption edges of amorphous $Al_{60}Ge_{30}Ni_{10}$ alloy. The weak bonding nature of Al-Ge atoms and the strong bonding nature of Ge-Ge and Al-Mn atoms are presumed from the equilibrium phase diagrams of Al-Ge with a wholly insoluble type of solid, and Al-Mn with many intermetallic compounds[19] and a covalent-type bonding of the Ge semiconductor. Furthermore, the new appearance of the small-angle peak at k_p=18.77 nm^{-1} suggests that the compositional short-range ordering consisting of Ge-Ge pairs with the strongest bonding force among the three constituent atoms developed on the scale of 0.3 to 0.4 nm. It has been clarified[20] that the irreversible structural change occurs accompanied by an exothermic heat of 1.8 kJ/mol upon continuous heating up to 570 K. Accordingly, the relaxation is presumably due to the local rearrangement of the constituent atoms leading to the development of compositional short-range ordering consisting of Ge-Ge and Al-Mn pairs with a strong bonding nature through the disappearance of Al-Ge pairs with a weak bonding nature, in addition to the annihilation of various kinds of quenched-in "defects". As demonstrated above, by using an Al-based alloy with an appropriate composition, it is possible, even by conventional X-ray diffractometry, to examine the annealing-induced change in the fraction of each pair of Al-M, Al-metalloid and metalloid-metalloid and the degree of compositional short-range ordering.

3. Hardness[2,17]

Figure 3-4 shows the change of Vickers hardness, H_v, as a function of M content for Al-Si-M (M=Cr, Mn, Fe, Co or Ni) and Al-Ge-M (M=Cr, Fe or Co) amorphous alloys with 25 %Si and 30 %Ge. H_v has a distinct M concentration dependence and increases with increasing M content from 365 to 600 at 10 %M to 730 to 1120 at 20 %M. The compositional

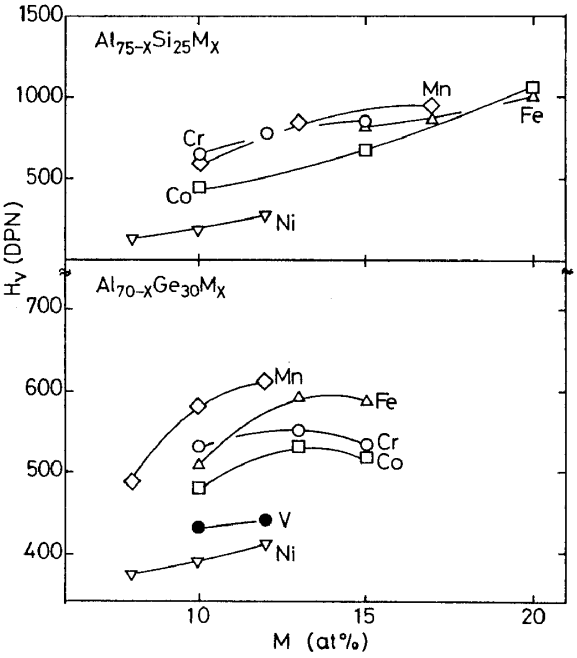

Fig. 3-4 Change in hardness (H_V) of Al-Si-M and Al-Ge-M (M=Cr, Mn, Fe, Co or Ni) amorphous alloys with M content.

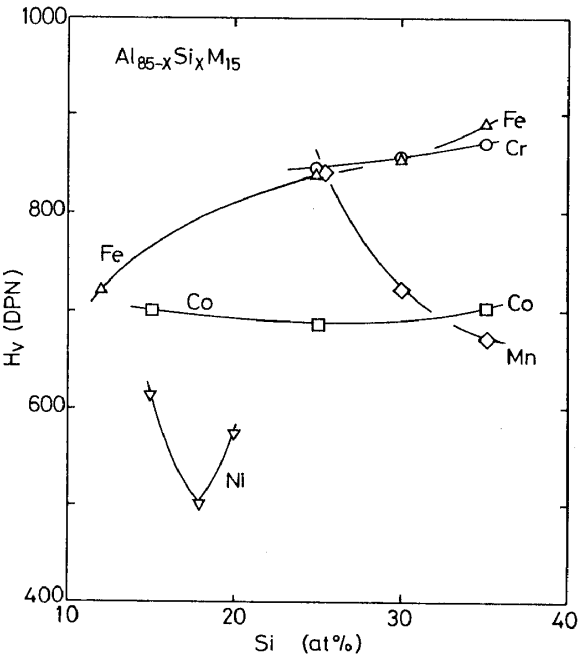

Fig. 3-5 Change in H_V of Al-Si-M (M=Cr, Mn, Fe, Co or Ni) amorphous alloys with Si content.

dependence of H_V is very similar in Al-Si-M and Al-Ge-M alloys. Figure 3-4 also shows that the H_V values of Al-Si-M and Al-Ge-M alloys are higher for the alloys with M=Cr, Mn or Fe than for the alloys with M=Ni or V and there is no appreciable difference in H_V between the alloys with M=Cr, Mn or Fe. It is notable that the H_V values at 20 %M may be as high as 700 to 1100 even for Al-based alloys, comparable to the high H_V values[21] for M-metalloid type amorphous alloys. Figure 3-5 shows the change of H_V as a function of Si content for Al-Si-M amorphous alloys with a constant M content of 15 %. The H_V values are independent of Si content and no distinct compositional dependence against the metalloid is also seen for Al-Ge-M alloys. Thus, the replacement of Al by M gives rise to significant increase in H_V for all the alloy systems, whereas the increase in H_V by the replacement of Al by Si or Ge is less significant. The bonding nature of the constituent atoms in Al-Si(or Ge)-M alloys increases in the order M-(Si or Ge) > Al-M > Al-(Si or Ge) from the data that T_m[19] and H_V[22] are larger for M-(Si or Ge) compounds than for Al-M compounds and no compound is formed in Al-(Si or Ge) alloys[19]. Accordingly, an increase in M content is presumed to bring about increase in H_V of the amorphous alloys, consistent with the results shown in Figs. 3-4 and 3-5.

4. Crystallization temperature (T_x)

T_x was also found to show a similar compositional dependence as that for H_v. As shown in Fig. 3-6, as the M content increases from 8 to 20 %, T_x increases from 498 to 715 K for Al-Si-(Cr, Mn, Fe or Co) alloys and from 370 to 575 K for Al-Si-Ni alloys. On the other hand, increase in T_x of Al-Ge-M alloys with increase in M content is considerably smaller than that of Al-Si-M alloys and the increase of T_x with increasing M content from 8 to 15 % is as small as about 50 K. Furthermore, T_x is higher by 50 to 150 K for Al-Si-M alloys than for Al-Ge-M alloys. This difference is probably because the eutectic temperature of Al-Si alloy is higher by 153 K than that of Al-Ge alloy[19]. The T_x values of Al-Si-M alloys are considerably higher for Al-Si-(Cr, Mn, Fe or Co) alloys than for Al-Si-Ni alloy and the Al-Si-M (M=Cr, Mn, Fe or Co) alloys have nearly the same T_x values. No distinct change in T_x with Si and Ge contents is observed as shown in Fig. 3-7. Thus, the H_v and T_x of Al-Si-M and Al-Ge-M amorphous alloys increase significantly with an increase in the amount of Al replaced by M, while those as a function of Si or Ge content do not show a significant change. Such compositional dependences probably occur because increasing M content results in an increase in the number of M-Si (or Ge) bondings with strongly attractive interaction and a decrease in the

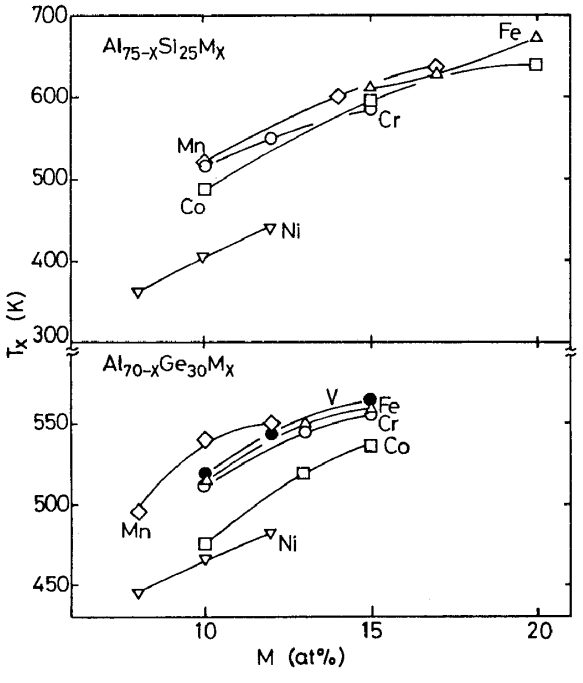

Fig. 3-6 Change in crystallization temperature (T_x) of Al-Si-M and Al-Ge-M (M=Cr, Mn, Fe, Co or Ni) amorphous alloys with M content.

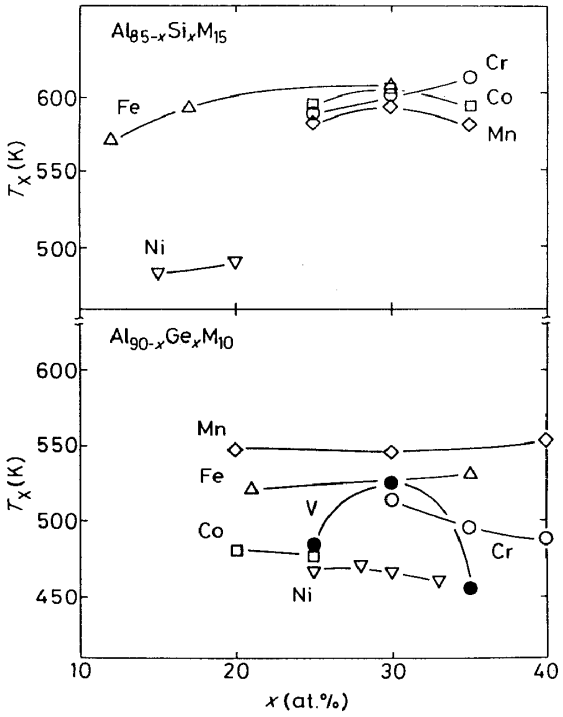

Fig. 3-7 Change in T_x of Al-Si-M and Al-Ge-M (M=Cr, Mn, Fe, Co or Ni) amorphous alloys with Si or Ge content.

number of Al-Si (or Ge) bondings with repulsive interaction. On the other hand, an increase in Si or Ge content does not cause a change in the number of M-Si (or Ge) bondings. Such a change as a function of metalloid content is significantly different from the general tendency[21] that H_v and T_x of M-metalloid amorphous alloys increase with increasing metalloid content. The significant difference is interpreted as due to the difference of bonding nature between M-Si (or Ge) atoms with strongly attractive interaction and Al-Si (or Ge) with repulsive interaction. Thus, it is said that the interaction of the consituent atoms for Al-based amorphous alloys is significantly different from that for M-metalloid type amorphous alloys reported previously, though the alloy compositions belong to the same category of metal-metalloid type.

5, Ductility and tensile fracture strength[2,17]

The Al-Si-Ni and Al-Ge-Ni amorphous alloys containing less than about 15 %Ni were found to exhibit a good ductility which is shown by a 180 degree bending without fracture. No ductile amorphous samples were obtained at the other alloy compositions in Al-(Si or Ge)-Ni systems and in the other alloy systems. Thus, the ductility is significantly dependent on the kind and concentration of M elements. The reason for such a good ductility only for Al-Si-Ni and Al-Ge-Ni amorphous alloys is presumably because the bonding nature of Ni-Al and Ni-Si (or Ge) pairs is the weakest among the bondings of M (M=Cr, Mn, Fe, Co or Ni) and Al, Si or Ge atoms. The results and discussion above are also consistent with the present presumption that the attractive bondings of M-Al and M-Si (or Ge) pairs play a dominant part in the glass formation.

Table 3-1 summarizes bending ductility, tensile fracture strength (σ_f), tensile fracture elongation (ε_f), H_v, T_x and heat of

Table 3-1 Mechanical properties, thermal stability and electrical properties for Al-Si-Ni and Al-Ge-Ni amorphous alloys.

Alloy (at %)	Ductility*	σ_f (MPa)	ε_f (%)	H_v (DPN)	T_x (K)	ΔH_x (kJ mol^{-1})	ϱ_{293} ($\mu\Omega$ cm)	TCR at 293 K (K^{-1})
$Al_{75}Si_{15}Ni_{10}$	D	440	1.4	370	465	2.80	150	–
$Al_{70}Si_{20}Ni_{10}$	D	375	1.2	295	400	2.95	170	-2.65×10^{-4}
$Al_{65}Si_{25}Ni_{10}$	D	–	–	265	405	3.60	300	-3.58×10^{-4}
$Al_{70}Si_{15}Ni_{15}$	B	–	–	610	510	2.90	230	–
$Al_{68}Si_{17}Ni_{15}$	B	–	–	485	500	3.25	410	–
$Al_{65}Si_{20}Ni_{15}$	B	–	–	570	505	3.20	660	–
$Al_{68}Si_{20}Ni_{12}$	D	–	–	435	440	2.90	340	–
$Al_{65}Ge_{25}Ni_{10}$	D	–	–	385	460	1.80	440	-1.10×10^{-3}
$Al_{60}Ge_{30}Ni_{10}$	B	–	–	390	470	1.70	1030	-2.06×10^{-3}

*D = ductile, B = brittle.

crystallization (ΔH_x) of Al-Si-Ni and Al-Ge-Ni amorphous alloys. The terms ductile and brittle distinguish success and failure in bending through 180 degrees. Although σ_f and ΔH_x are of the same order as those[23] of conventional amorphous alloys, σ_f, H_v and T_x are rather low presumably because of the weak bonding nature among the constituent atoms in the Al-rich alloys and low values of T_m, strength and hardness of Al metal itself.

6. Electrical resistivity[2,17]

Figures 3-8 and 3-9 show the change of electrical resistivity at room temperature (RT), ρ_{RT}, for Al-Si-M amorphous alloys with M and Si contents. The ρ_{RT} increases significantly with increasing M and Si contents and the increase is more remarkable for the increase in M content. The ρ_{RT} values lie in the range 220 to 1760 μΩcm which are two to six times higher than those (100 to 300 μΩcm)[24] for M-based amorphous alloys. A similar metalloid composition dependence of ρ_{RT} has also been recognized in $Al_{90-x}Ge_xM_{10}$ amorphous alloys[17]. The ρ_{RT} increases significantly from 500 to 850 μΩcm at 20 %Ge to 860 to 1940 μΩcm at 40 %Ge. Although the increase in ρ_{RT} with increasing Si or Ge content can be interpreted by taking the semiconducting nature of Si and Ge into consideration, the increase in ρ_{RT} with increasing M and Si or Ge contents is also thought to be related to the anomalous structure of the Al-based amorphous alloys. That is, as exemplified in Figs. 3-2 and 3-3, the X-ray and electron diffraction patterns of the Al-Si-M and Al-Ge-M amorphous alloys show split first halo peaks, the split being thought due to the phase separation into Al-rich and Si- or Ge-rich phases over a short range[2,20], i.e., the sites of Al and Si or Ge atoms in the amorphous structure are not random and are distributed in a distinguishable site on the scale of about 1 nm. It has been clarified[20] that the splitting phenomenon becomes significant with increasing M content. The split structure on a scale of about 1 nm is presumed to result in ρ_{RT} much higher than those of amorphous alloys with a homogeneously single structure.

Finally, the effect of M element on T_x, H_v and ρ_{RT} values of Al-Si-M and Al-Ge-M amorphous alloys is summarized in Figs. 3-10 and 3-11. T_x and H_v show a similar change; both values are the highest for alloys containing Cr, Mn and Fe and tend to decrease with decreasing group number in the periodic table. The systematic change as a function of the group number is interpreted as due to the bonding nature of M-Al, M-Si and M-Ge atomic pairs being stronger for the VI and VII group number elements. Additionally, the compositional effect of ρ_{RT} is thought to reflect the result that the number of conductive free

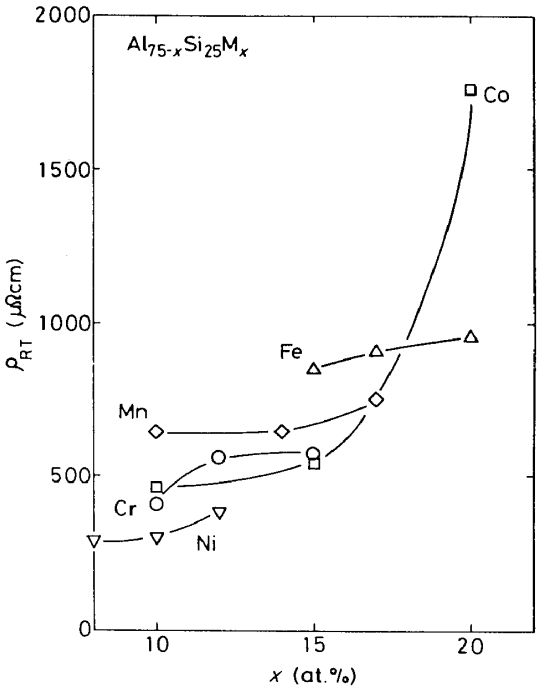

Fig. 3-8 Change in electrical resistivity at room temperature (ρ_{RT}) of $Al_{75-x}Si_{25}M_x$ (M=Cr, Mn, Fe, Co or Ni) amorphous alloys with M content.

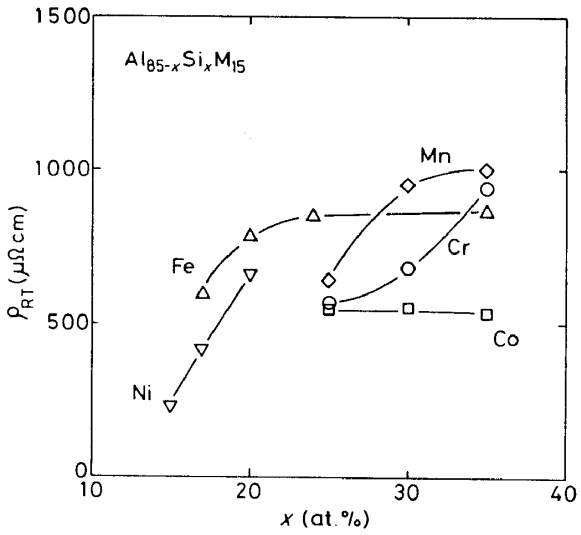

Fig. 3-9 Change in ρ_{RT} of $Al_{85-x}Si_xM_{15}$ (M=Cr, Mn, Fe, Co or Ni) amorphous alloys with Si content.

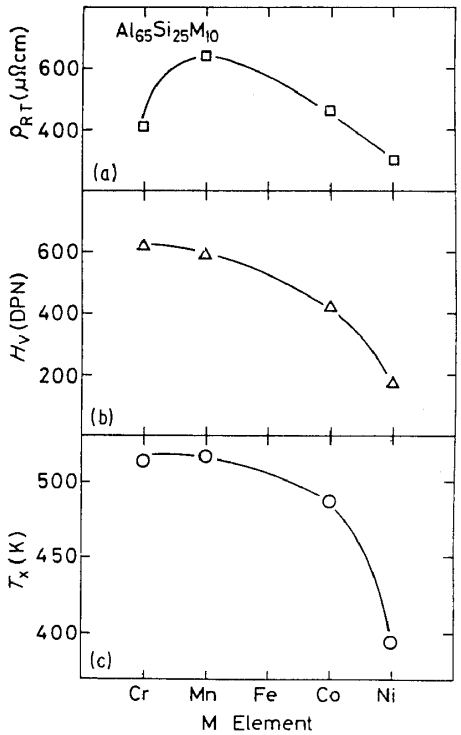

Fig. 3-10 Changes in ρ_{RT}, H_v and T_x of Al-Si-M amorphous alloys with the group number of M metals.

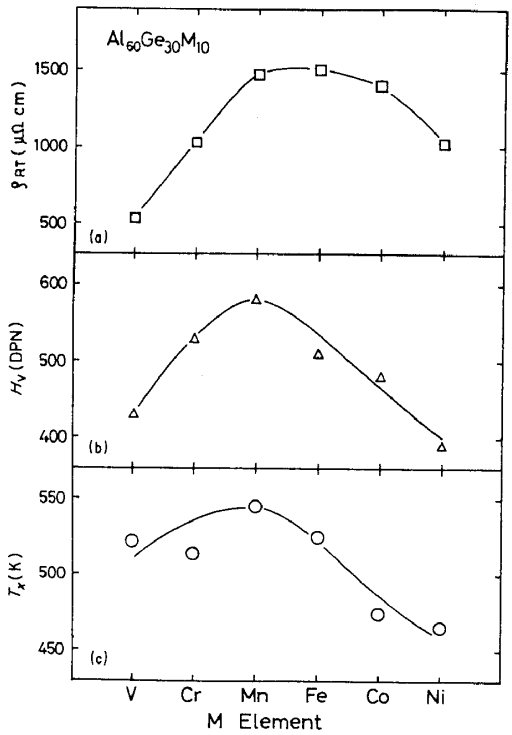

Fig. 3-11 Changes in ρ_{RT}, H_v and T_x of Al-Ge-M amorphous alloys with the group number of M metals.

electrons in the outer d-shell which do not contribute to the covalent bonding of M-Al, M-Si and M-Ge pairs is smaller for M=Cr and Mn and the hybridization between the d-band of the transition M metal and the s- and p-bands of Al is stronger for M=Cr and Mn[22].

IV. Al-EM-LM Amorphous Alloys

1. Amorphous alloy systems[10,11]

Figure 4-1 shows the effect of EM (EM=Ti, Zr, Hf, V, Nb, Ta, Cr, Mo or W) elements on the glass formation of $Al_{70}Fe_{20}M_{10}$, $Al_{70}Co_{20}M_{10}$, $Al_{70}Ni_{20}M_{10}$ and $Al_{70}Cu_{20}M_{10}$ alloys by melt spinning. The effectiveness of the M elements to form an amorphous phase is the greatest for Zr and Hf and decreases in the order of Ti > V > Mo > Nb > Cr >Ta. No amorphous phase was observed in the Al-based alloys containing W. Thus, alloys composed of the LM of Fe, Co, Ni and Cu, and the EM of Ti, Zr, Hf etc., and Al can form metal-metal type Al-based amorphous structures. It is also noteworthy that the formation of the amorphous alloys extends in rather wide compositional ranges surrounding the $Al_7(LM)_2(EM)_1$ compositions. For instance, the formation range extends from 5 to 35 %Cu and 5 to 15 %V for the Al-Cu-V system[25] and from 10 to 30 %Ni and 5 to 20 %Zr for the Al-Ni-Zr system[11].

The reason for the glass formation of the metal-metal type Al-based alloys is briefly discussed. The amorphous alloys are composed of Al, LM and EM. Furthermore, most of the binary alloys consisting of LM and EM except Al can be amorphized by melt spinning as exemplified for Fe-(Zr or Hf), Co-(Ti, Zr or Hf), Ni-(Ti, Zr or Hf) and Cu-(Zr or Hf)[18]. It has generally been known[18] that the amorphization of alloys is closely related to the ratio of T_g/T_m and the larger the ratio the higher is the glass-forming tendency. Although the T_m of Al-Cu alloys decreases with increasing Cu content in the range below 17.3 %, T_m of the other Al-M binary alloys rises very rapidly with increasing M content[19]. However, by the presence of the LM and EM, the rise in T_m of the Al-based ternary alloys is thought to be significantly depressed because many

M	Ti	Zr	Hf	V	Nb	Ta	Cr	Mo	W
$Al_{70}Fe_{20}M_{10}$	●	○	○	●	●	●	●	●	●
$Al_{70}Co_{20}M_{10}$	○	○	○	●	●	●	●	●	●
$Al_{70}Ni_{20}M_{10}$	○	○	○	○	○	◑	◑	○	●
$Al_{70}Cu_{20}M_{10}$	◑	○	○	○	●	●	◑	○	●

○ : Amorphous, ◑ : Amorphous+Crystalline, ● : Crystalline

Fig. 4-1 Effect of early transition M metals on the glass formation of $Al_{70}Fe_{20}M_{10}$, $Al_{70}Co_{20}M_{10}$, $Al_{70}Ni_{20}M_{10}$ and $Al_{70}Cu_{20}M_{10}$ (M=Ti, Zr, Hf, V, Nb, Ta, Cr, Mo or W) alloys by melt spinning.

eutectic points exist in the binary alloys of LM and EM[19]. In addition, a number of intermetallic compounds are formed in Al-M alloys as well as in EM-LM alloys[19]. It is therefore presumed that the attractive interaction among the constituent elements is significantly enhanced by adding the EM to the Al-LM binary alloys, leading to the increase in the viscosity of supercooled liquid and its temperature dependence which cause the enhancement of glass formation. The decrease of T_m and the increase of the attractive interaction among the constituent elements by the coexistence of Al, LM and EM appear to be dominant factors for the amorphization of the present metal-metal type amorphous alloys. On the other hand, the reason why no amorphization was observed in the alloy systems such as Al-(Fe, Co, Ni or Cu)-W and Al-(Fe or Co)-(V, Nb, Ta, Cr, Mo or W) etc. is probably because of the weak attractive interaction between LM and EM, as is evidenced from the existence of a wide solid solubility range in the binary alloys of LM and EM[19].

2. Thermal stability and hardness

Figures 4-2 and 4-3 show the changes in T_x, ΔH_x and H_v of the amorphous $Al_{70}Fe_{20}M_{10}$, $Al_{70}Co_{20}M_{10}$, $Al_{70}Ni_{20}M_{10}$ and $Al_{70}Cu_{20}M_{10}$ (M=Ti, Zr, Hf, V, Nb or Mo) alloys with M element. Considering the $Al_{70}Ni_{20}M_{10}$ alloys where the amorphization is achieved for various kinds of M elements, the values of T_x, ΔH_x and H_v in the same group number tend to increase with increasing atomic number while no systematic change in these values with group number is observed. Additionally, T_x and H_v decrease in the order of Fe > Co > Ni > Cu in $Al_{70}Fe_{20}M_{10}$, $Al_{70}Co_{20}M_{10}$, $Al_{70}Ni_{20}M_{10}$ and $Al_{70}Cu_{20}M_{10}$ amorphous alloys, suggesting that the bonding nature between Fe, Co, Ni or Cu and the other constituent elements decreases in the same order. This order agrees with the result[19] that the T_m of Al-rich Al-EM and

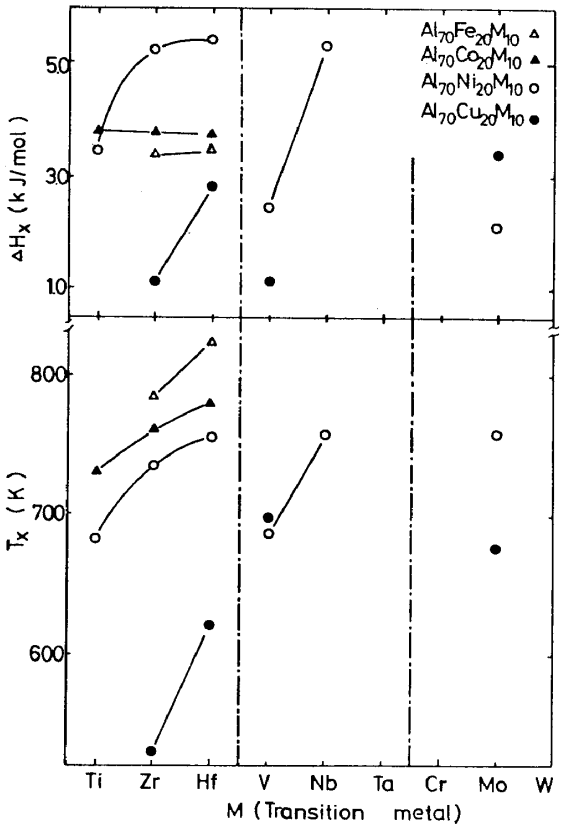

Fig. 4-2 Changes in T_x and heat of crystallization (ΔH_x) of $Al_{70}Fe_{20}M_{10}$, $Al_{70}Co_{20}M_{10}$, $Al_{70}Ni_{20}M_{10}$ and $Al_{70}Cu_{20}M_{10}$ amorphous alloys with early transition M metals.

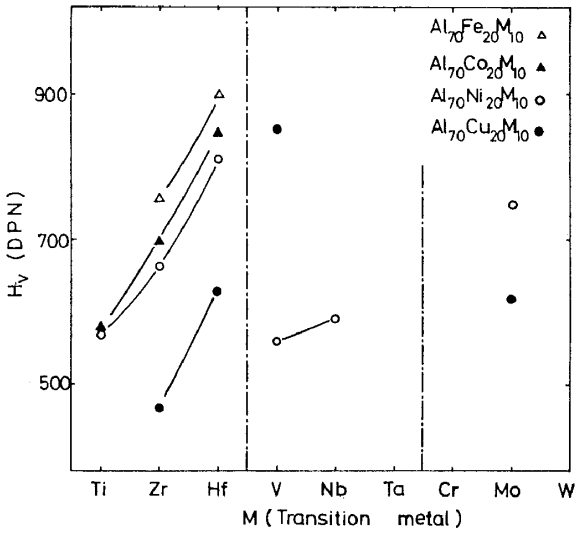

Fig. 4-3 Change in H_V of $Al_{70}Fe_{20}M_{10}$, $Al_{70}Co_{20}M_{10}$, $Al_{70}Ni_{20}M_{10}$ and $Al_{70}Cu_{20}M_{10}$ amorphous alloys with early transition M metals.

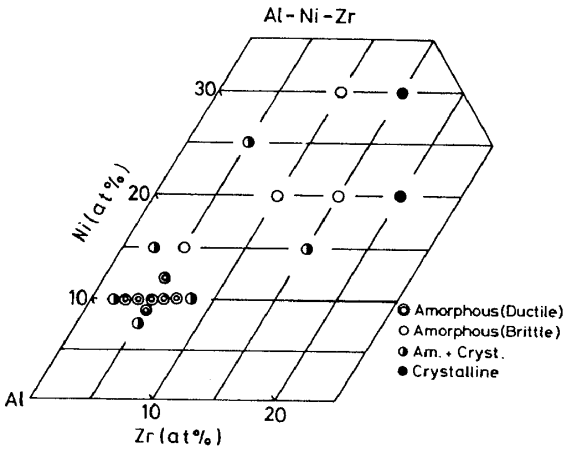

Fig. 4-4 Composition range and T_x in melt-spun Al-Ni-Zr alloys. (◎) amorphous (ductile); (○) amorphous (brittle); (◑) amorphous and crystalline; (●) crystalline.

Al-LM compounds and EM-LM compounds decrease in the order of Fe > Co > Ni > Cu. The highest values of T_x and H_V reach 825 K and 900 for $Al_{70}Fe_{20}Hf_{10}$, being comparable to those[26] for Fe-, Co- and Ni-based amorphous alloys.

3. Tensile fracture strength

In the Al-EM-LM amorphous alloys, the Al-Ni-Zr and Al-Ni-Hf alloys were found to be alloy systems with high glass-forming capacity and the easy amorphization enabled us to examine the compositional dependence of σ_f and Young's modulus (E). As an example, Fig. 4-4 shows the compositional range in which amorphous Al-Ni-Zr phase is formed by melt spinning, along with the data of T_x and bending ductility of the amorphous alloys. The glass formatin is in the range of 8 to 32 %Ni and 3 to 18 %Zr. It is notable that the amorphous alloys containing more than about 80 %Al can be completely bent through 180 degrees without fracture and no appreciable cracking is observed even at the severely deformed area. The ductility of the Al-Ni-Zr amorphous alloys is strongly dependent on the alloy composition and there is a clear tendency that the higher the Al content the higher is the ductility. On the other hand, T_x increases with decreasing Al content and shows the highest value (790 K) at 30 %Ni and 10 %Zr.

The σ_f, E, H_v and T_x of Al-Ni-Zr and Al-Ni-Hf amorphous alloys are summarized in Table 4-1, where the data of tensile fracture strain ($\varepsilon_f = \sigma_f/E$) and compressive yield strain ($\varepsilon_y \simeq H_v/3E$) is based on the fact that amorphous alloys exhibit liitle work-hardening and thus the compressive yield strength is related by $\sigma_y \simeq H_v/3$[27]. It can be seen in the table that the decrease in Al content gives rise to the increase

Table 4-1 Mechanical properties and thermal stability of Al-Ni-Zr amorphous alloys.

Alloy (at%)	T_x(K)	σ_f(MPa)	E(MPa)	H_v(DPN)	$\rho_{R.T.}$ ($\mu\Omega$cm)	$1/\rho_{R.T.}(d\rho/dT)$ (K^{-1})
$Al_{87}Zr_3Ni_{10}$	452	580	50000	280	-	-
$Al_{86}Zr_4Ni_{10}$	508	680	65700	330	340	5.23×10^{-5}
$Al_{86}Zr_5Ni_9$	489	750	72500	300	200	0.74×10^{-5}
$Al_{85}Zr_5Ni_{10}$	515	800	80400	340	460	0.97×10^{-5}
$Al_{85}Hf_5Ni_{10}$	560	730	75800	350	380	3.25×10^{-5}
$Al_{85}Nb_5Ni_{10}$	460	-	-	280	280	0.43×10^{-5}

from 580 to 800 MPa for σ_f, 50 to 80 GPa for E, 2740 to 3330 MPa for H_v and 452 to 515 K for T_x, indicating a similar compositional dependence in σ_f, E, H_v and T_x. Additionally, Fig. 4-5 shows the correlation between E and T_x, σ_f or H_v for Al-Ni-Zr amorphous alloys. The three properties of T_x, σ_f and H_v tend to increase with the increase in E. As shown in Table 4-1 and Fig. 4-5, the correlation between E and σ_f or H_v can be empirically expressed by the following approximate equations; $\varepsilon_f = \sigma_f/E \simeq 0.011$ and $\varepsilon_y \simeq H_v/3E \simeq 0.015$. The fracture behavior for the Al-Ni-Zr amorphous alloys is the same as those reported previously[28] for the other ductile amorphous alloys.

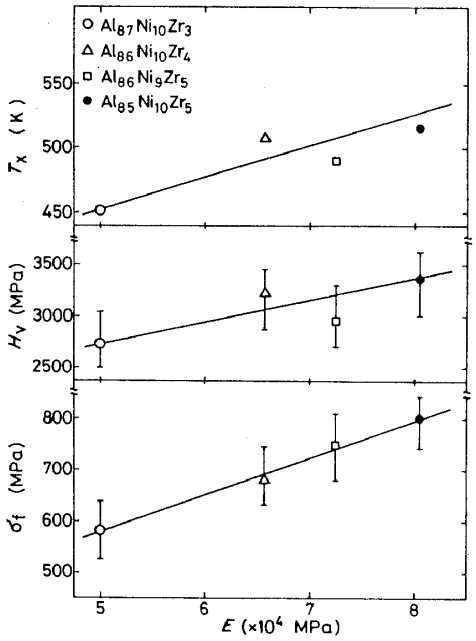

Fig. 4-5 Correlation between Young's modulus (E) and T_x, tensile fracture strength (σ_f) or H_v for Al-Ni-Zr amorphous alloys.

4. Electronic properties

The electrical resistivity of the ductile Al-Ni-Zr and Al-Ni-Hf amorphous alloys is in the range 200 to 460 μΩcm at room temperature and decreases almost linearly only by about 0.5 to 3.5 % with decreasing temperature to 4.2 K. A further decrease in temperature gives rise to the appearance of superconductivity at 2.05 K for $Al_{87}Ni_{10}Zr_3$ alloy. The temperature gradient of upper critical magnetic field H_{c2} near T_c is 0.20 T/K. The gradient value is about one-tenth as large as those (about 2.0 T/K)[29,30] for amorphous superconductors in Zr-, Nb- and Mo-based alloys. The significant difference is thought to reflect the difference in electrons contributing superconductivity, i.e., heavy d-electrons for the M-based amorphous alloys and s- and p-electrons for the Al-based amorphous alloys.

V. Al-Lanthanide Metal (Ln) Amorphous Alloys

1. Formation range of the amorphous alloys[14-16]

Figure 5-1 shows the compositional dependence of the as-quenched phase in the Al-Ln (Ln=Y, La, Ce, Pr, Nd, Sm, Gd, Tb, Dy, Ho, Er or Yb) binary systems. The amorphous phase is formed in compositional ranges 9 to 13 %Y, 7 to 11 %La or Ce, 10 %Pr, 8 to 12 %Nd or Gd, 8 to 16 %Sm, 9 to 14 %Tb and 9 to 12 % of Dy, Ho, Er or Yb. Thus, the glass-formation range is the widest for Al-Sm, followed by Al-Tb, Al-(Y, Nd or Gd), Al-(La, Ce, Dy, Ho, Er or Yb) and then Al-Pr. Furthermore, the supersaturated fcc solid solution is formed in the concentration ranges below the glass-formation ranges instead of an equilibrium mixture of fcc Al and intermetallic Al-Ln compounds. In the concentration ranges by about 1 at% higher than the glass-formation ranges, the quenching-induced phases are amorphous plus

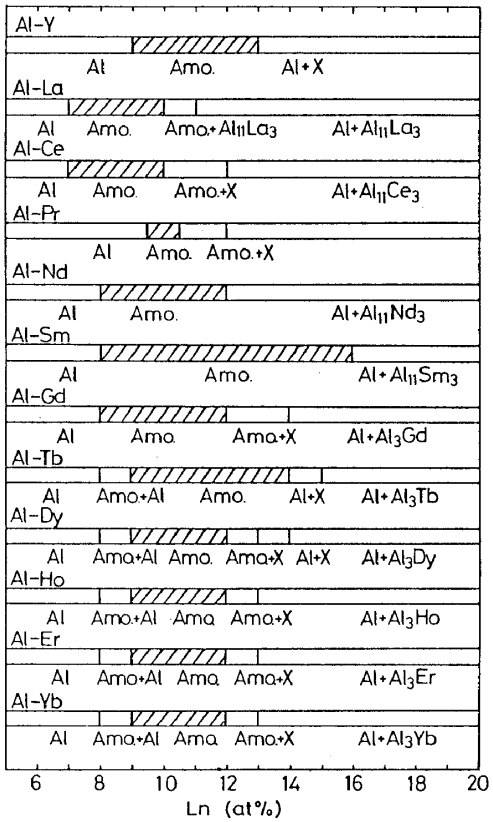

Fig. 5-1 Compositional dependence of structure in rapidly solidified Al-Ln (Ln=Y, La, Ce, Pr, Nd, Sm, Gd, Tb, Dy, Ho, Er or Yb) binary alloys.

unidentified x-phases in almost all the Al-Ln systems. A further increase of the solute concentration gives rise to the formation of equilibrium phases of either Al plus $Al_{11}Ln_3$ or Al plus Al_3Ln.

Figure 5-2 shows the relation between the glass-formation range and the equilibrium phase diagram[19] for the Al-Ln binary alloys. The glass-formation ranges except for the Al-Nd system lie in the compositional range between a eutectic point and $Al_{11}Ln_3$ (Ln=La, Ce, Pr, Nd or Sm) or Al_3Ln (Ln=Y, Gd, Tb, Dy, Ho, Er or Yb) compounds. Furthermore, the solidus temperature and the temperature difference between the liquidus and solidus points in their glass formation ranges are in the range of 625 to 655 K and 305 to 627 K, respectively. The melt-quenched phase at the eutectic composition with the lowest melting temperature is composed only of the fcc solid solution in all the alloy systems. This result is in disagreement with the previous tendency that the solute-poor amorphous alloys in metal-metal systems such as (Fe, Co or Ni)-Zr[31] and (Fe, Co or Ni)-Hf[32] etc., lie in the composition ranges including their eutectic points. The reason why the fcc single phase forms in place of an amorphous phase in spite of its trough of T_m near the eutectic composition is presumably because their eutectic compositions are too low to construct a stable amorphous structure.

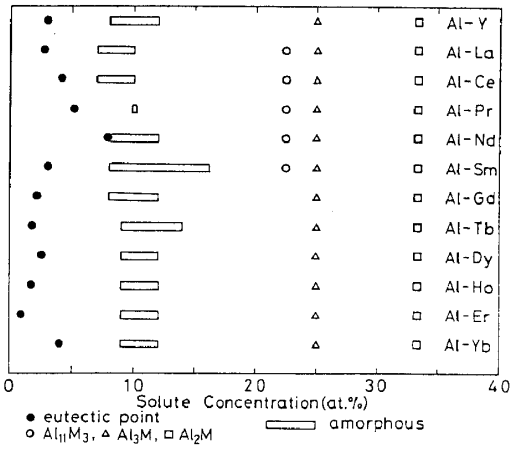

Fig. 5-2 Composition ranges for the formation of an amorphous phase in the Al-Ln (Ln=Y, La, Ce, Pr, Nd, Sm, Gd, Tb, Dy, Ho, Er or Yb) binary systems. Their binary phase diagrams were adopted from Ref.(19).

2. The reason for amorphization

We discuss the reason for the formation of the binary Al-Ln (Ln=Y, La, Ce, Pr, Nd, Sm, Gd, Tb, Dy, Ho, Er or Yb) amorphous alloys on the basis of the previous empirical factors for the glass formation of binary alloys by liquid quenching; namely, (1) the atomic size ratio of the constituent atoms is below about 0.8, and (2) the interaction between the constituent atoms is attractive and the mixing enthalpy is relatively large. Egami and Waseda[33] proposed the concept that the change from a crystalline solid solution to an amorphous phase in rapidly solidified alloys takes place when a volume mismatch due to the difference in atomic size exceeds a critical size factor (λ_o).

Furthermore, it has empirically been shown that the λ_o value is nearly equal to 0.1 for the binary amorphous alloys. Here, the λ_o value is given by the product of the minimum solute concentration (C_b^{min}) for the glass formation in a binary alloy system by liquid quenching and the volume mismatch of the constituent atoms (ΔV). The λ_o values at the minimum concentration for the Al-Ln alloys were claculated and summarized in Table 5-1 together with the data of C^{min}. As shown in Table 5-1, the λ_o values except that of Al-Yb alloy tend to decrease from 0.098 to 0.072 with increasing atomic number of the Ln metals because of the decrease in atomic size. The λ_o values for the Al-based alloys containing Ln metals with atomic numbers below 60 are in the range of 0.08 to 0.10, being roughly consistent with the empirical λ_o value of 0.1 for the glass formation. However, the λ_o values for the Al-Ln alloys containing heavier Ln metals except Yb are in the range below 0.08 and the Al-Yb alloy has a high value of 0.135 which deviates largely from the critical λ_o value ($\simeq$0.10), being inconsistent with the empirical rule. Furthermore, although the atomic size ratios of the Al-Ln alloys are in the range of 0.73 to 0.80 for Y, La, Ce, Pr, Nd, Sm, Gd or Yb, the ratios for the other Ln metals are larger than the empirical critical size ratio of 0.80 for the glass formation by liquid quenching. The inconsistency of the λ_o and atomic size ratio for the Al-Ln (Ln=Tb, Dy, Ho or Er) alloys indicates that the amorphization of the present binary alloys cannot be explained only by the empirical concept of the volume mismatch caused by the difference in atomic size.

It was pointed out in section IV that the attractive interaction between Al and M should be taken into consideration in the glass formation of Al-EM-LM such as Al-Ni-Zr, Al-Ni-Nb and Al-Ni-Hf etc., because the empirical critical size ratio of 0.8 is not satisfied in many Al-rich amorphous alloys belonging to the Al-EM-LM system. It is reasonable to consider that the concept of the attractive interaction can be also applied to the interpretation of the glass formation of the present Al-Ln alloys. Although there are no

Table 5-1 The minimum solute concentration (C_b^{min}) for the glass formation in the Al-Ln (Ln=Y, La, Ce, Pr, Nd, Sm, Gd, Tb, Dy, Ho, Er or Yb) binary alloys by liquid quenching, the volume mismatch between Al and Ln atoms (ΔV) and the critical size factor (λ_o) obtained by the product of C_b^{min} and ΔV.

Ln metal	C_b^{min}	ΔV	λ_o
Y	0.09	1.062	0.096
La	0.07	1.272	0.087
Ce	0.07	1.096	0.077
Pr	0.09	1.096	0.098
Nd	0.08	1.062	0.084
Sm	0.08	0.961	0.077
Gd	0.08	0.929	0.083
Tb	0.09	0.864	0.078
Dy	0.09	0.833	0.075
Ho	0.09	0.833	0.075
Er	0.09	0.802	0.072
Yb	0.09	1.497	0.135

measured data of the mixing energies between Al and Ln metals, the enthalpy of mixing for Al-Y and Al-La alloys has theoretically been predicted[34] to be -131 and -109 kJ/g-atom, respectively. In addition, the equilibrium phase diagrams[19] of the Al-Ln binary alloys indicate that intermetallic compounds with high melting temperatures exist at Al-rich compositions and the solute concentrations and melting temperature, which reflect the magnitude of attractive interaction (mixing energy) between Al and Ln metals, are in the range of 21.4 to 25 at% and 1253 and 1723 K, respectively. The minimum solute concentrations (21.4 to 25 at%) for formation of the Al-rich compounds are equal to or lower than that of Al-M binary alloys, and the melting temperatures of $Al_{11}Ln_3$ and Al_3Ln compounds are higher than those (973 to 1217 K) of Al-rich compounds (Al_4Ca and Al_9Co_2) with solute concentrations below 25 at%. These data allow us to conclude that the magnitude of attractive interaction between Al and Ln metals is larger for Ln metals than for the other solute metals. Accordingly, it may be concluded that the glass formation in Al-Ln binary alloys by liquid quenching results mainly from a strong attractive interaction of the constituent elements rather than the volume mismatch by the difference in the atomic size ratio. The enhancement of the glass-forming capacity by the increase of the attractive interaction of the constituent atoms is probably because the diffusivity of the constituent atoms in the supercooled liquid region becomes difficult and the temperature dependence of viscosity becomes steep for the supercooled liquid.

3. Amorphous structure

The structure of an $Al_{90}Y_{10}$ amorphous alloy was examined[35] by anomalous X-ray scattering (AXS) at the Y and Ni K-absorption edges using synchrotron radiation at the Photon Factory of the National Laboratory for High Energy Physics, Tsukuba Japan. Details of the experimental setting and analysis are explained in [36]. Figure 5-3 shows the scattering intensities measured at 17.0126 and 16.7380 keV below the Y K-absorption edge in the binary $Al_{90}Y_{10}$ alloy. The fundamental features of both profiles are typical for noncrystallinity. A distinct feature observed in these profiles is a pronounced prepeak at Q=13 nm^{-1}, which is indicated with an arrow in the figure. In general, the prepeak is qualitatively interpreted as indicating compound-formation, and the partial structure factor of unlike-atom pairs in this type of disordered alloys is found to show a very sharp first peak with a prepeak[37,38]. It may be noted that similar profiles were observed in other amorphous Al-based alloys, such as Al-Si-Mn and

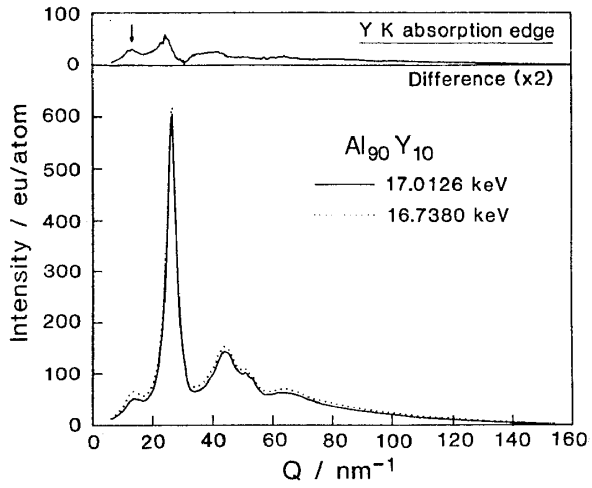

Fig. 5-3 Differential intensity profile of amorphous $Al_{90}Y_{10}$ (top) determined from the intensity profiles (bottom) measured at incident energies of 17.0126 and 16.7380 keV, which correspond to energies of 25 and 300 eV below the Y K-absorption edge. The arrow indicates the prepeak.

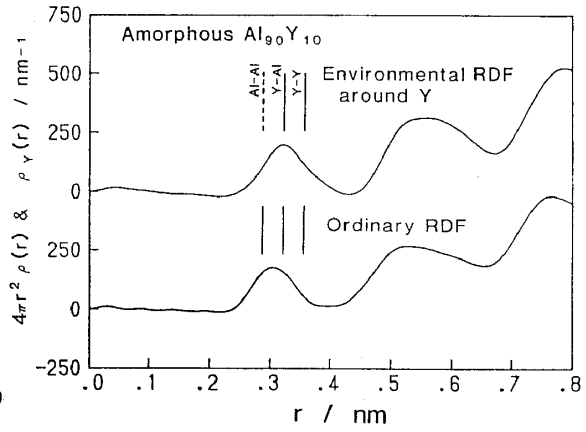

Fig. 5-4 Environmental radial distribution function (RDF) around Y (top) and ordinary RDF (bottom) of amorphous $Al_{90}Y_{10}$ (density=2.87 g/cm^3).

Al-Mn[39,40]. The differential intensity profile at the Y K-edge, calculated by taking the difference between the two intensity profiles, is shown at the top of Fig. 5-3. The prepeak is still observed in the differential profile, which again implies the presence of a certain local ordering formed by the Y and Al atoms. The Fourier transform of this differential profile gave the environmental RDF around Y, which is shown at the top of Fig. 5-4. The ordinary RDF, which is given at the bottom of Fig. 5-4, was also computed from the intensity measured at 17.0126 keV.

Both RDFs indicate an almost completely resolved first peak and rather prominent oscillations over a wide range of r, compared with the RDF of a typical amorphous alloy. This type of atomic configuration in disordered systems corresponds to distinct local near neighbor correlations as seen in semiconducting liquids and oxide glasses, accompanied by a complete loss of correlation between such local units at larger distances[41]. Thus, certain short-range clusters, which are different from those normally obtained in a random mixture of constituents are present in amorphous $Al_{90}Y_{10}$.

The distances of atomic pairs Al-Al, Al-Y and Y-Y computed from the tabulated metallic bonding distances[42] are indicated in the figure. In $Al_{90}Y_{10}$, the ordinary RDF is the sum of three partial RDFs of Al-Al,

Al-Y and Y-Y pairs, and the environmental RDF around Y contains only two partial RDFs of Al-Y and Y-Y pairs. With this fact in mind, the first peak of the ordinary RDF is considered to be due to Al-Al, Al-Y and Y-Y pairs, whereas the first peak of the environmental RDF around Y is likely expressed by a correlation of Al-Y and Y-Y pairs. This is clearly supported by the observation that the peak caused by the correlation of Al-Al pairs disappears in the environmental RDF, and by the rather spread first peak of the ordinary RDF formed mainly by Al-Al and Al-Y pairs with a small contribution from the Y-Y pairs. In the environmental RDF, the maximum of the first peak and a tail extending to longer r are found to correspond to the computed distances of Al-Y and Y-Y pairs, respectively. Thus, it is expected that Y atoms are mainly surrounded by Al atoms instead of Y atoms. Coordination numbers and distances for these pairs are estimated by fitting this first peak with Gaussian's at approximate bonding distances. The coordination numbers of Al and Y around Y determined from the environmental RDF are 14.1 and 1.1, respectively. The large coordination numbers of Al around Y may be explained by considering that the size of a Y atom is about 20 % larger than that of an Al atom. Using the values determined in the environmental RDF around Y, the coordination number and atomic distance for Al-Al pairs are determined from the first peak of the ordinary RDF. The results are summarized in Table 5-2. From this table it is found that more than 92 % of the near-neighboring atoms of Y are Al atoms, which indicates that the Y atoms are almost completely surrounded by Al atoms since the atomic fraction of Al is 0.9.

There is an empirical relation between the correlation length, r, in real space and the peak position, Q, in the intensity profile, i.e., Qr=2.5 in molten transition metals and metalloid alloys[41]. It is

Table 5-2 Coordination numbers, N, and interatomic distances, r, for amorphous $Al_{90}Y_{10}$, experimentally determined from the first peaks of the ordinary RDF and the environmental RDF around Y.

Amorphous $Al_{90}Y_{10}$				
Pairs	Ordinary RDF		Environmental RDF around Y	
	r/nm	*N*	*r*/nm	*N*
Al-Al	0.288	10.7±0.8		
Al-Y	0.320	1.6±0.2		
Y-Al	0.320	14.2±1.3	0.320	14.1±1.5
Y-Y	0.362	1.2±0.9	0.362	1.1±0.4

plausible that this relation is also valid in the amorphous state. Thus, the correlation length causing the prepeak at 13 nm^{-1} is estimated to be 0.60 nm, which agrees well with the distance between neighboring Y atoms bonded through an Al atom. Consequently, these experimental results prove the presence of Y atoms surrounded by Al atoms in binary $Al_{90}Y_{10}$ alloy.

4. Thermal stability[16)]

Figure 5-5 shows onset temperature of the first exothermic peak (T_x) as a function of Ln content for the Al-Ln amorphous alloys. With increasing Ln content from 7 to 12 at%, T_x increases significantly from 434 to 534 K and no further increase of T_x is seen in the Ln concentration range of 12 to 16 at%. Thus, the compositional effect of T_x is almost independent of the atomic number of the Ln elements, though the Al-Er and Al-Yb alloys exhibit lower T_x values. In order to clarify the reason for the significant increase of T_x for the Al-Ln amorphous alloys with increasing Ln content from 7 to 12 at%, crystallization behavior was examined for some Al-Ln amorphous alloys. As examples, Fig. 5-6 shows differential scanning calorimetric curves of amorphous $Al_{100-x}Tb_x$ and $Al_{100-x}Dy_x$ (x=9, 10, 11 and 12 at%) alloys. Two or three exothermic peaks are seen on the DSC curves, indicating that the crystallization takes place through two or three stages. From

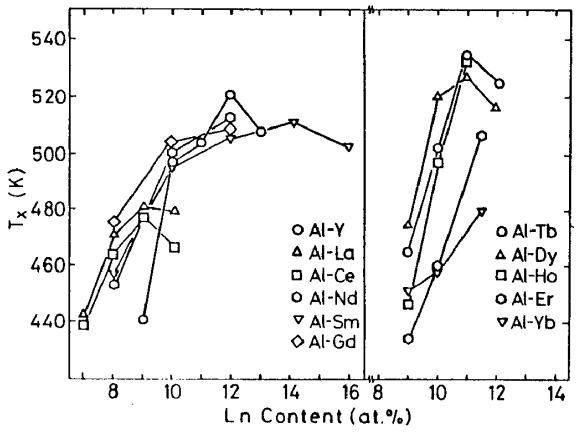

Fig. 5-5 Crystallization temperature (T_x) of amorphous Al-Ln (Ln=Y, La, Ce, Pr, Nd, Sm, Gd, Tb, Dy, Ho, Er or Yb) alloys as a function of Ln content.

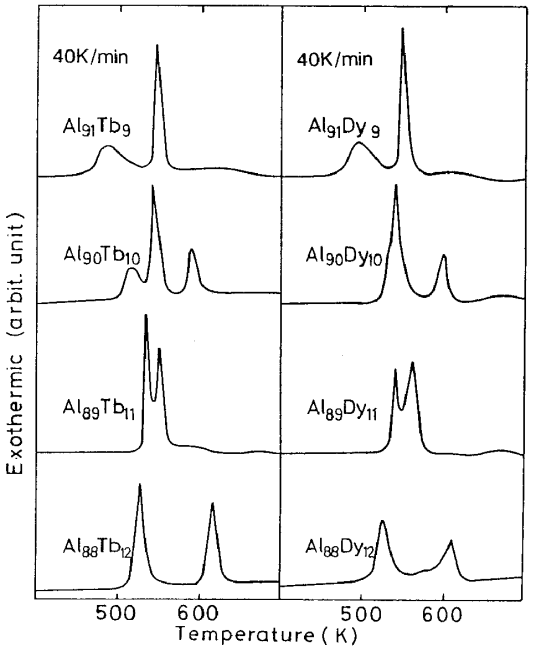

Fig. 5-6 Differential scanning calorimetric curves of amorphous $Al_{100-x}Tb_x$ and $Al_{100-x}Dy_x$ (x=9, 10, 11 and 12 at%) alloys.

the X-ray diffraction analyses, it was confirmed that the broad exothermic peak at the low-temperature side for $Al_{91}Tb_9$, $Al_{90}Tb_{10}$ and $Al_{91}Dy_9$ alloys is due to the precipitation of fcc Al and the second exothermic peak is due to the precipitation of Al, x and Al_3Tb or Al_3Dy phases from the remaining amorphous phase. The increase of T_x by the disappearance of the Al phase is also seen for the other Al-Ln (Ln=Y, La, Ce, Nd or Sm) amorphous alloys. Accordingly, the strong compositional dependence of T_x shown in Fig. 5-5 is due to the disappearance of fcc Al phase resulting from the change of the crystallization process of Am. → Am.+Al → Al+Al_3Ln to Am → Al+x+Al_3Ln → Al+Al_3Ln or Am. → Al+Al+Al_3Ln.

5. Mechanical properties

Figure 5-7 shows the change of H_v as a function of Ln content for the Al-Ln amorphous alloys. The H_v shows an almost linear dependence in the entire compositional range and increases significantly from 150 to 270 for the Al-Ln alloys. Although the Al-Sm, Al-Dy and Al-Tb amorphous alloys exhibit higher H_v values, no systematic change in H_v with the atomic number of the Ln elements is seen for the Al-Ln amorphous alloys. Here, it is important to describe that all the amorphous alloys in the Al-Ln binary system have a good ductility which is shown by a 180 degree bending without fracture. Figure 5-8 shows the change of σ_f as a function of Ln content for the Al-Ln amorphous alloys. The σ_f increases significantly from 360 to 870 MPa with increasing Ln content. It should be noted that all the amorphous alloys in the Al-Ln systems exhibit tensile strengths which exceed the highest value (530 MPa) obtained in optimumly age-hardened Al-base alloys. The fracture surface appearance was also examined for Al-Ln amorphous ribbons fractured by the uniaxial tensile test and the fracture behavior was confirmed to be just the same as that for conventional ductile amorphous alloys.

6. The reason for the compositional dependence of mechanical strengths

It was described in section V-2 that the attractive bonding nature between Al and Ln metals plays an important role in the glass formation of Al-Ln binary alloys. Furthermore, the structural data described in section V-3 indicate that the coordination number of Al atoms around Y atoms is about 1.4 times as large as the average value expected from the atomic concentration of the alloy and hence the short-range ordering of Al-Y pairs develops homogeneously in the Al-Y amorphous phase. The formation of the short-range ordered structure is presumably due to the strongly attractive interaction between Al and Y

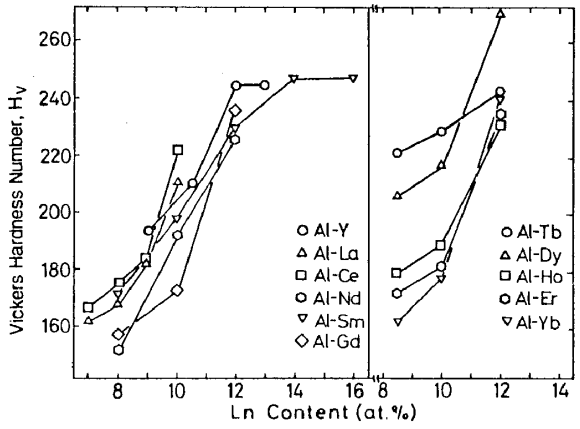

Fig. 5-7 Hardness (H_v) of amorphous Al-Ln (Ln=Y, La, Ce, Pr, Nd, Sm, Gd, Tb, Dy, Ho, Er or Yb) alloys as a function of Ln content.

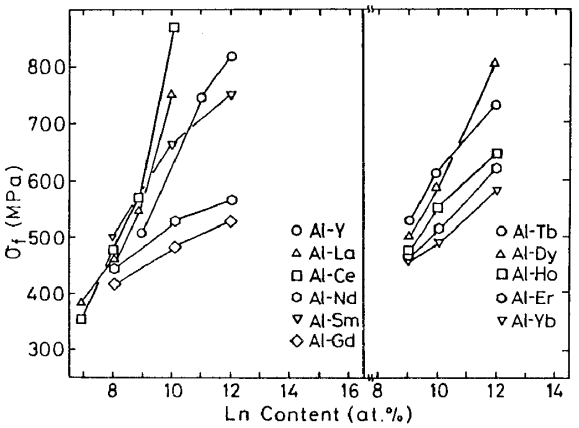

Fig. 5-8 Tensile fracture strength (σ_f) of amorphous Al-Ln (Ln=Y, La, Ce, Pr, Nd, Sm, Gd, Tb, Dy, Ho, Er or Yb) alloys as a function of Ln content.

atoms. It is therefore reasonable to consider that the number of the attractive Al-Y pair in the Al-Y amorphous alloys increases linearly with increasing Y content, leading to the linear increase of mechanical strengths. This presumption is consistent with the result in which the σ_f and H_v values of the Al-Ln amorphous alloys increase almost linearly with increasing Ln content and are independent of the atomic number of the Ln metals. In other words, the high strengths of the Al-Ln binary amorphous alloys seem to result from the Al-Ln bonding with strong attractive interaction and the remarkable increase of σ_f and H_v is due to the increase of the number of the Al-Ln bonding. Furthermore, the attractive bonding nature between Al and Ln metals is probably due to a high hybridization tendency between s-p electrons in Al and f-d electrons in Ln metals.

It was shown that all the properties of T_x, H_v, σ_f and ρ_{RT} for the Al-Ln amorphous alloys were independent of the atomic number of the Ln metals. The atomic size of the Ln metals varies systematically with the atomic number and hence the atomic size factor also seems to have little effect on the above-mentioned properties. On the other hand, it is generally known that the inherent chemical nature of the Ln metals results from 4f electrons which lie at the inner side in their atoms. Although the number of the 4f electrons varies systematically with the atomic number, the electrons are screened by $5s^2$ and $5p^6$ electrons which lie at the outer side of the atoms, resulting in a similarity in chemical properties of the Ln metals. Accordingly, it may reasonably be assumed that the independence of the properties of the Al-Ln amor-

phous alloys as a function of atomic number is due to the unique electronic structure in which the 4f electrons are screened by 5s and 5p electrons.

Similarly, the disappearance of the primary Al phase with increasing Ln content in the crystallization process of the Al-Ln amorphous alloys is explained on the basis of the decrease of the number of Al atoms which do not bond with Ln metals. The suppression of the primary Al phase gave rise to a rapid increase of T_x. However, the increase of the number of the Al-Ln pairs seems to bring about an ease of the precipitation of the Al-Ln compounds, resulting in almost saturated T_x values at high Ln concentrations in the Al-Ln amorphous alloys shown in Fig. 5-5.

7. Electrical resistivity[14-16)]

Figure 5-9 shows the temperature dependence of electrical resistivity in the range of 77 K to room temperature for amorphous $Al_{90}Ln_{10}$ (Ln=Nd, Sm, Gd, Tb, Dy, Ho, Er or Yb) alloys. It can be seen for all the amorphous alloys that the resistivity change is positive in the entire temperature range and almost linear at temperatures above 150 K. As the Ln content increased from 8 to 12 at%, the resistivity at room temperature was measured to increase from 48-65 to 76-109 μΩcm. Furthermore, the temperature coefficient of resistivity defined by $1/\rho_{RT}(d\rho/dT)$ for the $Al_{90}Ln_{10}$ amorphous alloys is in the range of 0.134×10^{-4} to 6.29×10^{-4} K^{-1}. Thus, the feature of the resistivity behavior is also independent of the atomic number of the Ln elements.

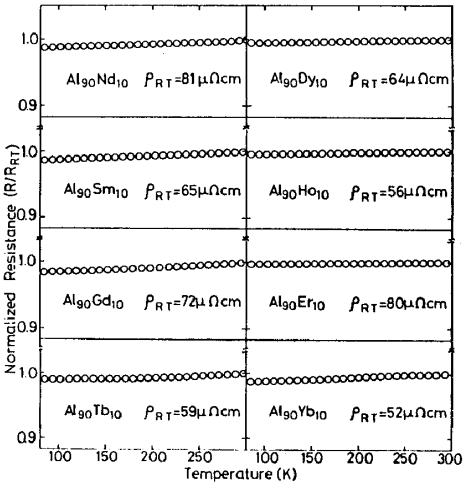

Fig. 5-9 Electrical resistivity of amorphous Al-Ln (Ln=Nd, Sm, Gd, Tb, Dy, Ho, Er or Yb) alloys as a function of temperature.

8. The reason for the compositional dependence of electrical resistivity

As described in section V-7, the electrical resistivity at room temperature for the Al-Ln amorphous alloys increases significantly from 48 to 109 μΩcm with increasing Ln content from 8 to 12 at%. Furthermore, it has previously been reported[43)] that the Hall coefficient (R_H) at room temperature for the Al-Y amorphous alloys is negative and the magnitude increases from 22×10^{-12} to 32×10^{-12} m^3/As with increasing Y

content. From the increase in the magnitude of the negative R_H, it is interpreted that the number of the free electrons contributing to electrical conductivity decreases with increasing Y content, if one assumes the relation of $R_H=-1/(Nne)$ which can be derived from the nearly free electron model. Here, N is the atomic density and n is the number of electrons per atom. The strongly attractive interaction between Al and Ln atoms suggests that the s and p electrons in Al metal hybridize with f- and d-electrons in Ln metals, leading to the decrease of the free electrons which are attributed to electrical conductivity. As a result, the increase of the number of the Al-Ln pairs in Al-Ln amorphous alloys with increasing Ln content gives the significant increase in electrical resistivity and in magnitude of the negative R_H.

As described in this section, the glass formation of the Al-Ln binary alloys and the compositional dependences of σ_f, H_v, ρ_{RT} and R_H are explained by the common concept that the Al-Ln pairs with attractively bonding nature are formed preferentially in the Al-Ln amorphous alloys and the s and p electrons in Al hybridize tightly with the 4f and 5d electrons in the Ln metals.

VI. Al-Lanthanide Metal(Ln)-Transition Metal(M) Amorphous Alloys

1. Formation range of the amorphous alloys[12,13]

Figure 6-1 shows the compositional ranges in which amorphous Al-Y-M, Al-La-M and Al-Ce-M (M=Fe, Co, Ni or Cu) phases are formed by melt spinning. The formation ranges of Al-Y-M and Al-Ce-M amorphous alloys are the widest for the Al-Y-Ni and Al-Ce-Ni systems; no distinct difference is seen among the other three alloys in the Al-Y-M and Al-Ce-M systems, while those for the Al-La-M amorphous alloys are the narrowest for the Al-La-Cu system and much wider for the other Al-La-(Fe, Co or Ni) systems. Accordingly, the effectiveness of M elements on the compositional range for formation of the Al-based amorphous alloys

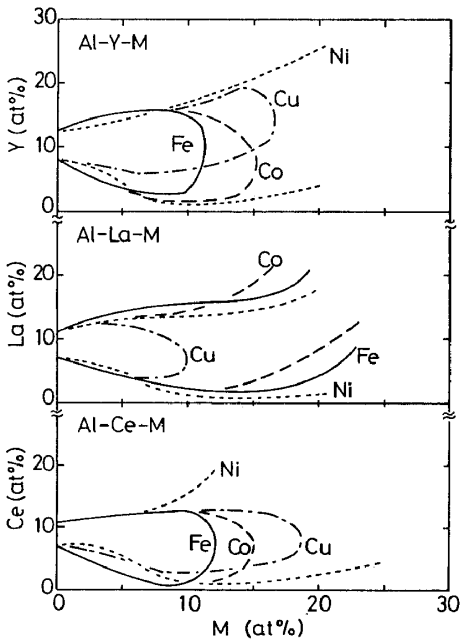

Fig. 6-1 Compositional range for formation of amorphous phase in Al-Y-M, Al-La-M and Al-Ce-M systems.

is the greatest for Ni, followed by Fe, Co and then Cu. These amorphous alloys containing more than about 80 %Al can be completely bent by 180 degrees without fracture, and no appreciable crack is observed even in the severely deformed area. The ductility of the Al-Ln-M amorphous alloys is strongly dependent on alloy composition and there is a clear tendency such that the higher the Al content, the higher the ductility.

2. Amorphous structure[35)]

Intensity profiles measured at the Y K-absorption edge in amorphous $Al_{87}Y_8Ni_5$ and their difference are shown in Fig. 6-2. These intensity profiles are similar to those (Fig. 5-3) observed in the binary $Al_{90}Y_{10}$. They also include the prepeak at about 13 nm^{-1}. Thus, the structural features of the ternary alloy seem to be similar to those of the binary alloy. For this ternary alloy, the environmental RDF around Y as well as the ordinary RDF shown in Fig. 6-3 were estimated. As drawn in the RDFs of Fig. 5-4, the nearest neighbor distances of pairs calculated from the metallic bonding distances of Al, Y and Ni are indicated in the figure. The ordinary RDFs of $Al_{90}Y_{10}$ and $Al_{87}Y_8Ni_5$ are compared at the bottom of Fig. 6-3. The solid and dotted curves correspond to the RDFs of the ternary and binary alloys, respectively. It is found that the first peak of the ternary alloy extends to lower r than that of the binary alloy. By comparing the peak positions with

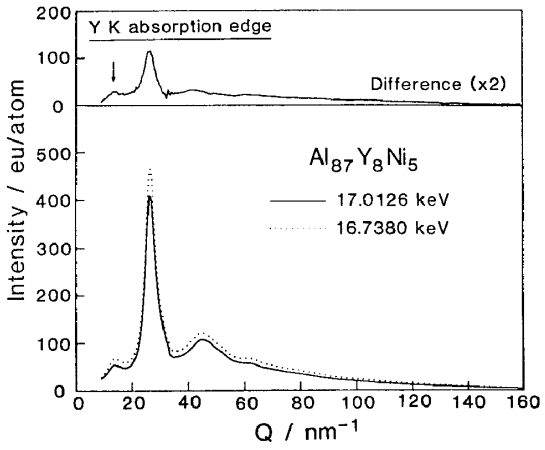

Fig. 6-2 Differential intensity profile of amorphous $Al_{87}Y_8Ni_5$ (top) determined from the intensity profiles (bottom) measured at incidence energies of 17.0126 and 16.7380 keV, which correspond to energies of 25 and 300 eV below the Y K-absorption edge. The arrow indicates the prepeak.

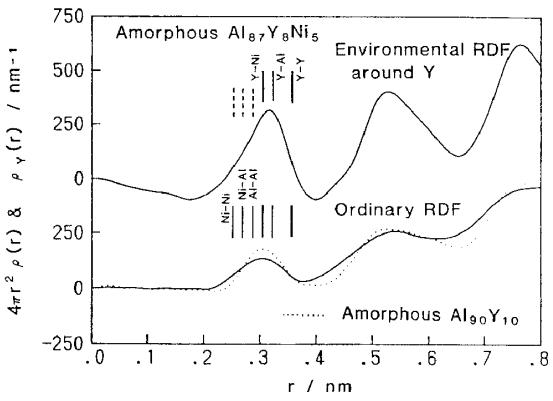

Fig. 6-3 Environmental RDF around Y (top) and ordinary RDF (bottom) of amorphous $Al_{87}Y_8Ni_5$ (density=3.09 g/cm^3).

the calculated bonding distances of the pairs, it is found that this tail at the lower r side corresponds to Ni-Ni and Ni-Al pairs which are not included in the binary Al-Y alloy. The environmental RDF around Y contains three partial RDFs of Y-Ni, Y-Al and Y-Y. This is clearly seen in the profiles of the first peaks of the RDFs in Fig. 6-3. The atomic positions of pairs unrelated with Y disappear in the environmental RDF around Y. A tail at lower r of the first peak in the environmental RDF around Y of the Al-Y-Ni alloy, which is not observed in the environmental RDF around Y of the Al-Y alloy, appears to be due to the correlation of Y-Ni pairs. Gaussian fitting of the first peak of the environmental RDF in Fig. 6-3 gave the coordination numbers and atomic distances of the Y-Ni, Y-Al and Y-Y pairs. Considering the coordination number and its error for Y-Y, the Y-Y pairs are again insignificant in this ternary alloy. These results are summarized in Table 6-1. From these results, about 16 % of the atoms surrounding a Y atom are found to be Ni, which is much more than the value expected from the Ni concentration. It suggests that the local ordering structure formed in the ternary alloy included Ni as well as Al and Y.

In $Al_{87}Y_8Ni_5$, the AXS measurements were also carried out around the Ni K-absorption edge. The scattering profile of the ternary alloy measured at 8.3067 and 8.0316 keV, which are the energies of 25 and 300 eV below the Ni K-absorption edge, respectively, and their difference are shown in Fig. 6-4. In this intensity difference a prepeak, indicated with an arrow in the figure, is still observed at about 13 nm^{-1}. A similar prepeak was observed in the intensity difference at the Y K-absorption edge in Fig. 6-2. These prepeaks in the differential intensity profiles at the Ni and Y K-absorption edges support the results of the environmental RDF around Y discussed above, i.e., the presence of clusters consisting of the three constituent elements. The environmental RDF around Ni obtained from the Fourier-

Table 6-1 Coordination numbers, N, and interatomic distances, r, for amorphous $Al_{87}Y_8Ni_5$, experimentally determined from the first peaks of the ordinary RDF and the environmental RDF around Y.

Amorphous $Al_{87}Y_8Ni_5$				
Al-Ni	0.268	6.5 ± 0.2		
Ni-Al	0.268	0.4 ± 0.1		
Al-Al	0.286	7.2 ± 0.8		
Ni-Y	0.303	3.5 ± 2.6		
Y-Ni	0.303	2.2 ± 1.7	0.297	2.7 ± 0.7
Al-Y	0.320	1.2 ± 0.2		
Y-Al	0.320	13.5 ± 2.7	0.320	14.3 ± 1.9
Y-Y	0.356	0.8 ± 0.6	0.356	0.4 ± 0.4

transform of the differential intensity profile is inserted in the figure. As shown in Fig. 6-4, the AXS data of the Ni K-absorption edge are restricted to a wavevector Q range up to about 76 nm^{-1}, arising from the relatively low energy absorption edge (8.333 keV) of Ni. This prevents us to obtain the accurate environmental RDF around Ni due to the finite termination in the Fourier transformation, compared with the AXS data of the Y K-edge. Therefore, the information of the Ni environment is less quantitative than that for the Y environment. A careful interpretation is required for the environmental RDF around Ni, which is the sum of the three partial RDFs of Ni-Ni, Ni-Al and Ni-Y. The nearneighbor distances of the Ni-Ni, Ni-Al and Ni-Y pairs computed from the bonding distances are indicated in the figure. The first peak of the environmental RDF around Ni seems to be mainly due to Ni-Al and Ni-Y pairs, the contribution of Ni-Ni pairs to the first peak being small. Thus, the tail at lower r of the first peak in the ordinary RDF was only fitted with Ni-Al pairs. Based on these results of the environmental RDFs around Ni and Y, the first peak of the ordinary RDF was fitted with Ni-Al, Al-Al, Ni-Al, Al-Y and Y-Y pairs. The resultant coordination numbers and atomic distances are summarized in Table 6-1.

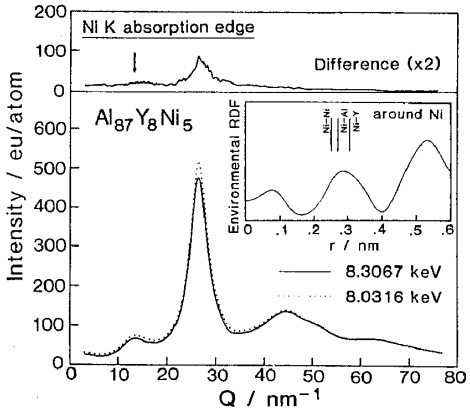

Fig. 6-4 Differential intensity profile of amorphous $Al_{87}Y_8Ni_5$ (top) determined from the intensity profiles (bottom) measured at incidence energies of 8.3067 and 8.0316 keV, which correspond to energies of 25 and 300 eV below the Ni K-absorption edge. The arrow indicates the prepeak. The environmental RDF around Ni is inserted in the figure.

Fractions of occupancy for the constituent elements around Al in the near-neighbor region are estimated. The values for Al, Y and Ni are about 82, 14 and 4 %, respectively. The value for Al is smaller than its concentration while the value of Y is larger than its concentration. This suggests that there is a strong interaction between Al and Y. On the other hand, it is noteworthy that the value of Ni is almost equal to its concentration. Similarly, fractions around Y were computed. Ni atoms occupy about 14 % in the near-neighbor region around Y, and the rest is mostly occupied by Al. The value for Ni is much higher than the number expected from the Ni concentration. This indicates a strong interaction between Y and Ni. From these results it is concluded that Al atoms surrounding Y in the binary Al-Y alloy are

preferably replaced by Ni atoms in the ternary Al-Y-Ni alloy and a local ordering is formed by the three elements. This is consistent with the result concluded from the environmental RDF around Y. It is inferred from the prepeak of the environmental RDF around Y in the binary alloy that the prepeak at about 13 nm^{-1} in both the environmental RDFs of the ternary alloys represents the atomic correlation between Y and Al or Ni.

The A-Y and Al-Ni systems have a very shallow eutectic in the Al-rich region. Then, it is rather surprising that this Al-Y-Ni alloy can be amorphized by melt quenching. The formation of the local ordering structures observed in the present study would facilitate the glass formation in these alloys. As described later, the fracture strength of amorphous alloys is much higher than that of crystalline metals and approaches the theoretical strength, and yet their ductility is high. Thus, most of the attractive mechanical properties of high fracture strength and ductility in the ternary amorphous Al-Y-Ni alloys may be attributed to the particular structural features of the amorphous phase. As-spun Al-Ge-Ni alloys, which form an amorphous phase over a wide range of concentration[2,17], do not show good mechanical properties. The structural analysis of an amorphous $Al_{60}Ge_{30}Ni_{10}$ alloy by ordinary X-ray diffraction and AXS technique[44] disclosed that its structure is a mixture of Ni-rich highly ordered crystal-like regions and Ge-rich regions. This contrasts to the present Al-Y-Ni alloy structure. Therefore, the homogeneity of the amorphous phase seems to be another factor to improve its mechanical properties.

3. Electrical resistivity (ρ_{RT}) and Hall coefficient (R_H)

Figure 6-5 shows the ρ_{RT} of $Al_{90-x}Fe_xLn_{10}$ (Ln=Y or La) as a function of the Fe content. It is observed that the ρ_{RT} increases rapidly with Fe content. The increase in the Al-Fe-La system is not as pronounced as in the Al-Fe-Y system. Therefore, a marked difference which depends on the two Ln species is observed. The effect of substituting Co for Al on the ρ_{RT} and R_H for $Al_{90-x}Co_x$(Y or La)$_{10}$ is shown in Fig. 6-6 (a) and (b). The ρ_{RT} increases with the concentration of M as we have already seen

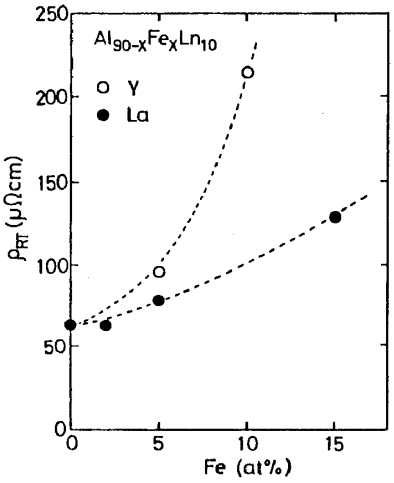

Fig. 6-5 Fe concentration dependence of ρ_{RT} for melt-spun amorphous $Al_{90-x}Fe_x$-Ln_{10} alloys.

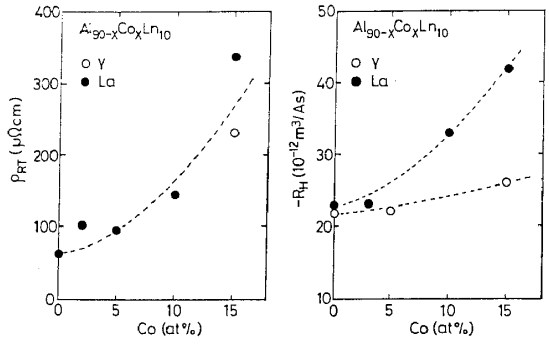

Fig. 6-6 Co concentration dependence of the ρ_{RT} (a) and R_H (b) for melt-spun amorphous $Al_{90-x}Co_xLn_{10}$.

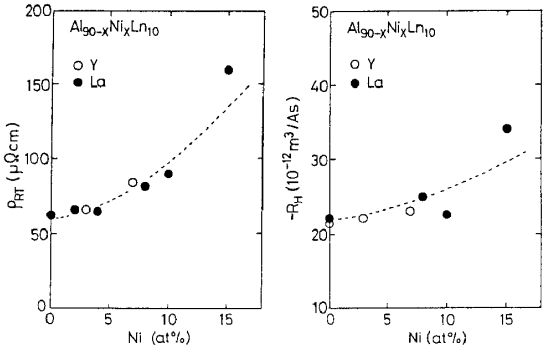

Fig. 6-7 Ni concentration dependence of the ρ_{RT} (a) and R_H (b) for melt-spun amorphous $Al_{90-x}Ni_xLn_{10}$ alloys.

in Fig. 6-5, but in this case it is independent of the nature of the Ln element. In contrast to the similarity in the resistivity behavior, the R_H, which is found to be negative for all the alloys studied here, is found to depend on the alloyed Ln element. However, the general feature is that as the solute content increases the magnitude of the R_H also increases. Figure 6-7(a) and (b) shows the concentration dependence of ρ_{RT} and R_H for amorphous Al-Ni-Ln alloys with 10 %Ln (Ln=Y or La). The observed dependencies on Ni concentration are quite similar to those on Co substitution except that in the present alloys both R_H and ρ_{RT} do not seem to depend on Y or La.

Figure 6-8(a) and (b) show the ρ_{RT} and R_H of $Al_{90-x}Co_{10}(Y \text{ or } La)_x$ as a function of the Ln content. It is observed that the ρ_{RT} increases rapidly from about 90 to 220 $\mu\Omega$cm with 13 % substitution of Ln, almost parabolically with Ln content but it is independent of the Ln elements. The magnitude of the R_H is also seen to increase rapidly with the content of Ln independent of whether Y or La is substituted. In

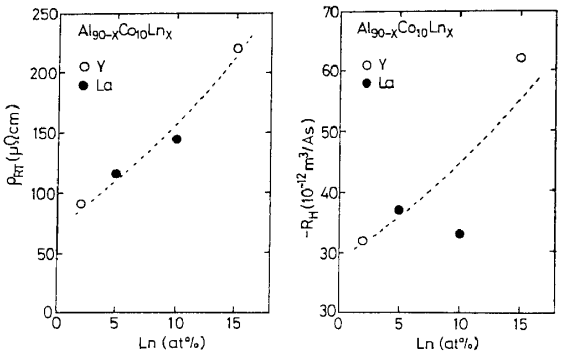

Fig. 6-8 Ln concentration dependence of the ρ_{RT} (a) and R_H (b) for melt-spun amorphous $Al_{90-x}Co_{10}Ln_x$ alloys with Ln=Y or La.

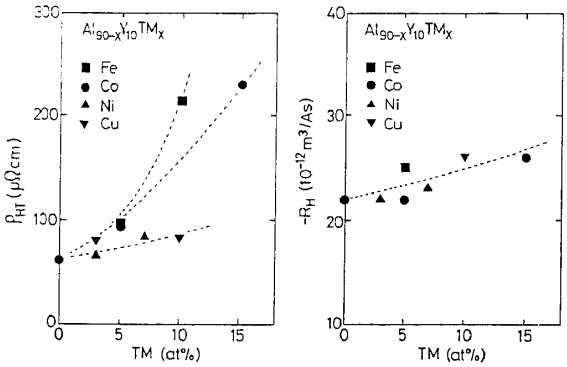

Fig. 6-9 ρ_{RT} (a) and R_H (b) for melt-spun amorphous $Al_{90-x}M_xY_{10}$ with M=Fe, Co, Ni or Cu.

addition, Fig. 6-9(a) and (b) show the ρ_{RT} and R_H data for $Al_{90-x}M_xY_{10}$ (M=Fe, Co, Ni or Cu). Similar data were also obtained for the Al-M-La alloys. It is easily seen from Fig. 6-9 that the ρ_{RT} increases with M content, in a manner already noted before. This increase is more pronounced in the alloys containing Fe and Co (in that order), while for Ni and Cu substitution the ρ_{RT} is almost constant. However, the increase in the magnitude of the R_H appears not to depend on the nature of the M element.

4. The reason for the compositional dependence of ρ_{RT} and R_H[43)]

The electronic properties of simple metal amorphous alloys are expected to behave according to the free-electron model since the spatial isotropy that should exist in homogeneous amorphous alloys would lead to a spherical Fermi surface. However, substitution of Al by Ln and/or M species raises the fundamental question as to how the free-electron-like behavior expected for Al will be altered by the presence of other atoms with a very different electronic structure and atomic size. The two Ln species examined in this work, Y and La, have a very similar atomic radius and the same outer electronic structure, namely (d^1s^2), thus substitution of 10 at% of Al by any Ln element should essentially produce similar changes in the electronic properties. Indeed this is what we observe experimentally: For example, within the limits of experimental error both $Al_{90}La_{10}$ and $Al_{90}Y_{10}$ present an electrical resistivity of 66 μΩcm and an ordinary R_H -22.5×10^{-12} m^3/As. In a free-electron model it will be expected that the R_H of these two alloys shows an almost free-electron value, given by $R_H=-1/(Nne)$. Assuming three conduction electrons per Al and Y (or La) atoms, the equation gives a R_H of -38×10^{-12} m^3/As. This is almost twice the experimental value. On the other hand, it has been shown that La-based amorphous alloys have positive R_H[45)] and for liquid La the value of $R_H=+61.5\times10^{-12}$ m^3/As[46)] has been reported. We now discuss the effects of M elements on partial substitution of Al.

The Hall-effect data (Fig. 6-9(b)) indicate that there is a decrease in the carrier density when increasing the M content probably because of the formation of additional Al-M bonds in addition to the existence of Al-Ln. Thus, while the progressive formation of local Al-M covalent bonds seems to result in a decrease in the effective free-electron concentration irrespective of the nature of the M, the $_{RT}$ strongly suggests that s-d scattering contribution decreases with Fe, Co and Ni, in that order, as expected from the d-state occupation in these elements. The Cu atom has its 3d band filled and thus no (s,p)-d scattering is expected to contribute to the ρ_{RT} which will be

determined by (s,p) electrons. On the other hand, the Fe and Co atoms with an incomplete 3d band offer a more complex situation. In this case both the formation of covalent bonds and a larger probability for the conduction electrons of Al to be scattered into d states of the M atoms contribute to an increase of the ρ_{RT}. An X-ray photoemission spectroscopy study of LM dissolved in Al[47] indicates that there is an hybridization of the 3d electrons of the M with the conduction electrons (s,p) of Al which lead to a density of states in the Fermi level characterized by (s,p) electrons, the 3d band of the M atoms lying well below the Fermi level. The hybridization will enhance (s,p)-d scattering in agreement with the present measurements. This would explain, in part, the additional contribution and different rates of increase of the ρ_{RT} as being due to s-d scattering from Fe, Co, Ni and Cu. However, it is necessary to point out that the total change in the magnitude of the ρ_{RT} from about 65 μΩcm to as high as 250 μΩcm or more in the amorphous state for a change in concentration of the additional elements by about 15 at% is unusual. Such large changes in ρ_{RT} are not observed with compositional changes of the order of 20 at% in d-band amorphous materials rich in M components[48].

Despite the negative values observed for the R_H in all the studied alloys and the increase in magnitude when Al is substituted by M and Ln indicating a decrease in the density of carriers we have shown that a free-electron model is not quantitatively applicable even though the large concentration of Al might suggest it. This fact suggests that s-d scattering which is assumed to contribute to the ρ_{RT} may also be important in order to understand quantitatively the R_H for these alloys.

4. Superconducting properties[49]

Figure 6-10 shows the normalized electrical resistance $R/R_{4.2}$ for amorphous $Al_{85}La_{7.5}M_{7.5}$ (M=Zr, Nb, Mo, Ni or Cu) alloys. The transition into a superconducting state occurs sharply with a temperature width of less than 0.3 K. The transition temperature (T_c) defined by 50 % of $R_{4.2}$ increases from 2.56 to 4.02 K in the order of Ni < Cu < Zr < Mo < Nb and no superconductivity at temperatures above 1.5 K is detected for the corresponding alloys containing Ca or Fe. There is a tendency for the T_c values to be higher for the alloys containing the M elements of the fifth period of the periodic table as compared to the fourth period elements and T_c decreases significantly by the dissolution of magnetic elements. It is notable that the T_c values of the Al-based amorphous alloys are much higher than that (0.9 K)[50] of pure Al metal. From the expectation of high T_c in the amorphous Al-La-Nb

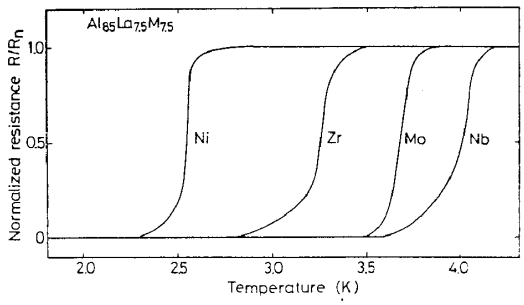

Fig. 6-10 Normalized electrical resistance, R/R_n, as a function of temperature for $Al_{85}La_{7.5}M_{7.5}$ (M=Zr, Nb, Mo, Ni or Cu) amorphous alloys.

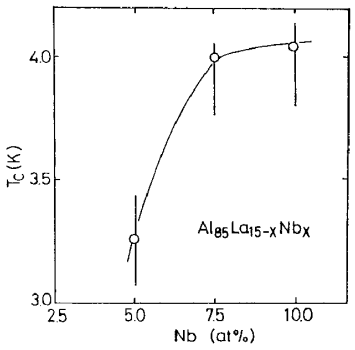

Fig. 6-11 Change in T_c for $Al_{85}La_{15-x}Nb_x$ amorphous alloys with Nb content.

system, the compositional change of T_c was examined for $Al_{85}La_{15-x}Nb_x$ alloys. As shown in Fig. 6-11, the T_c value increases from 3.25 to 4.07 K with an increase of Nb content from 5 to 7.5 % and then becomes nearly constant.

It is known that the compositional dependence of T_c for amorphous alloy superconductors containing M of the fourth and fifth period as major elements is closely related to the change in the average number of outer electrons per atom (e/a). The strong correlation between T_c and e/a has been named as the Collver-Hammond rule[51] for amorphous superconductors and T_c shows a maximum value at e/a=6.4 for the 4d transition metals and alloys. The T_c values as a function of e/a for $Al_{85}La_{7.5}M_{7.5}$ alloys are shown in Fig. 6-12. One can notice a maximum value of T_c at e/a=3.15, being significantly different from the Collver-Hammond rule. Furthermore, the previous empirical rule suggests that the T_c value is higher for $Al_{85}La_{7.5}Mo_{7.5}$ than for $Al_{85}La_{7.5}Nb_{7.5}$, but the suggestion is inconsistent with the present result. This inconsistency suggests that the contribution of Al metal must be taken into consideration for the interpretation of the present superconductivity.

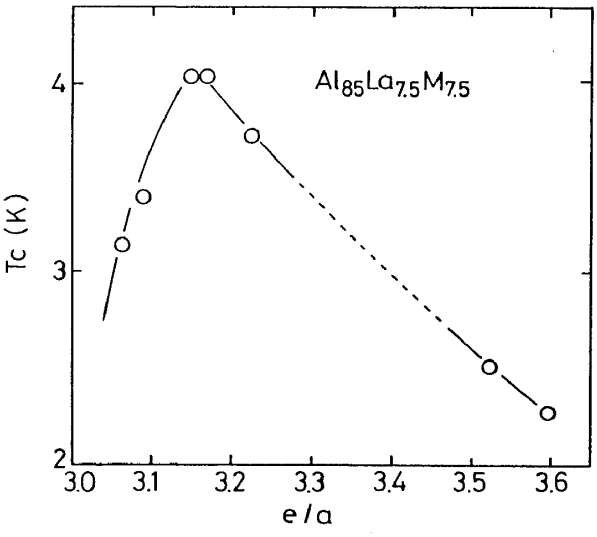

Fig. 6-12 Change in T_c for $Al_{85}La_{7.5}M_{7.5}$ (M=Zr, Nb, Mo, Ni or Cu) amorphous alloys with e/a.

Figure 6-13 shows the temperature dependence of H_{c2} for $Al_{85}La_{7.5}M_{7.5}$ amorphous alloys.

Here, H_{c2} is defined to be the applied magnetic field at which the resistance of the samples reaches a half of its normal value. H_{c2} increases linearly with lowering temperature in the range above $t=T/T_c=0.58$ to 0.72, but it shows negative deviation from the linear relation at low temperatures. The temperature gradient of H_{c2} near T_c, $-(dH_{c2}/dT)_{Tc}$ increases in the range of 0.221 to 0.308 T/K in the order of Cu < Ni < Zr < Nb < Mo. It is notable that the gradients are about a tenth of the values (1.5 to 3.0 T/K)[29,30] for amorphous alloy superconductors in M-based system. The H_{c2} value at 1.8 K is in the range 0.40 to 0.57 T which are much lower than those for the other amorphous superconductors because of the much lower $(dH_{c2}/dT)_{Tc}$ values. A strong correlation between T_c and e/a for the Al-based amorphous superconductors shown in Fig. 6-12 is thought to be attributed to the change in $N(E_f)$ with e/a. The electronic dressed density of states at the Fermi level, $N^*(E_f)=N(E_f)(1+\lambda)$, was estimated from the measured values of the H_{c2} gradient near T_c, $-(dH_{c2}/dT)_{Tc}$, and normal electrical resistivity at 4.2 K, $\rho_{4.2}$, by using the following formula which is derived from the Ginzburg-Landau-Abrikosov-Gorkov (GLAG) theory (e.g., [52]) and is applicable for the dirty-type superconductor of the Al-La-M amorphous alloys:

$$N(E_f)(1 + \lambda) = -\pi/[8k_B\rho_n(dH_{c2}/dT)_{Tc}] \qquad (1)$$

As shown in Table 6-2, the values of $N(E_f)(1 + \lambda)$ thus obtained tend to increase from 0.24×10^{47} to 0.66×10^{47} in the order of Ni < Zr < Nb ≃ Mo as does T_c, suggesting that T_c is dominated by $N(E_f)$ and/or λ. The problem which parameter, $N(E_f)$ or λ, dominates the change in T_c with M elements remains unsolved within the present study and investigation on the low-temperature specific heat is in progress to determine the most dominant factor.

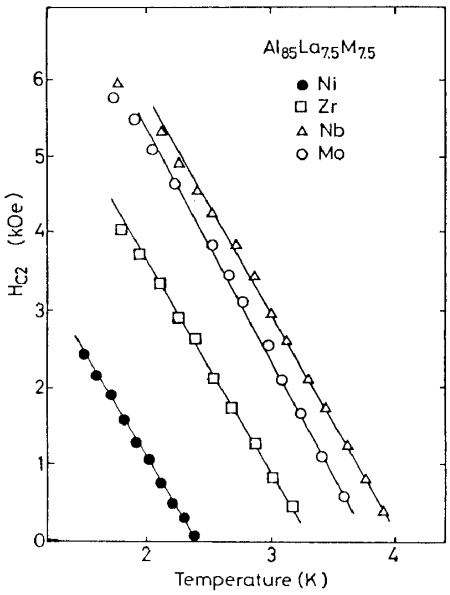

Fig. 6-13 The upper critical magnetic field H_{c2} at various temperatures for $Al_{85}La_{7.5}M_{7.5}$ (M=Zr, Nb, Mo or Ni) amorphous alloys. The solid lines represent a linear extrapolation at T_c.

It was shown in Fig. 6-13 that the gradient of H_{c2} in the vicinity of T_c for the Al-La-M amorphous alloys is about 10 % of that[29,30] of

Table 6-2 Thermal stability and electrical and superconducting properties of $Al_{85}La_{7.5}M_{7.5}$ (M=Zr, Nb, Mo, Ni or Cu) amorphous alloys.

Alloy	T_x(K)	$\rho_{4.2}$(μΩcm)	T_c (K)	ΔT_c(K)	H_{c2}(kOe/K)	$-(dH_{c2}/dT)_{T_c}$(kOe/K)	$N^*(E_f)$
$Al_{85}La_{7.5}Zr_{7.5}$	430	142	3.26	0.30	4.01	2.70	0.33
$Al_{85}La_{7.5}Nb_{7.5}$	488	86	4.02	0.24	5.54	2.91	0.61
$Al_{85}La_{7.5}Mo_{7.5}$	511	96	3.71	0.19	5.70	3.08	0.66
$Al_{85}La_{7.5}Ni_{7.5}$	559	185	2.56	0.11	1.60	2.45	0.24
$Al_{85}La_{7.5}Cu_{7.5}$	496	90	2.04	—	—	—	—

amorphous alloy superconductors in M-based systems. The equation (1) indicates that the gradient is dominated by ρ_n, $N(E_f)$ and λ. One of the reasons for the extremely low gradient values is probably the low electrical resistivities which are about 50 % of those (200 to 300 μΩcm)[24,53] for the M-based amorphous superconductors. Furthermore, it is known that Al metal with T_c at 0.9 K has 3s- and 3p-electrons in the outer shell, which are different from the 3d- and 4d-electrons for the M-based alloys, and belongs to a weak coupling superconductor with a low λ value ($\simeq 0.38$)[54]. The different type of outer electrons and the low λ value appear to be another reason for the small temperature gradient of H_{c2} for the Al-La-M amorphous alloys.

5. Thermal stability[12,13,55]

In order to clarify the compositional dependence of thermal stability for the Al-Y-M, Al-La-M and Al-Ce-M amorphous alloys, T_x values are plotted as a function of M (M=Fe, Co, Ni or Cu) content in Fig. 6-14 and as a function of Ln (Ln=Y, La or Ce) content in Fig. 6-15. T_x values of the Al-based alloys without Cu element have a distinct compositional dependence and increase significantly with an increase of Fe, Co, Ni, Y, La or Ce content, i.e., from 528 to 724 K for $Al_{90-x}Y_{10}M_x$, 544 to 793 K for $Al_{90-x}La_{10}M_x$, 500 to 730 K for $Al_{90-x}Ce_{10}M_x$, 414 to 750 K for $Al_{90-x}Y_xM_{10}$, 486 to 740 K for $Al_{90-x}La_xM_{10}$ and 402 to 620 K for $Al_{90-x}Ce_xM_{10}$. There is no distinguishable difference in the compositional dependence of T_x among Al-Y-M, Al-La-M and Al-Ce-M alloys. The effect of M elements on the increase of T_x tends to decrease in the order of Fe > Co > Ni and no distinct change in T_x with Cu is seen for either the Al-Y-Cu or Al-La-Cu alloy.

The structural skeleton in the Al-based amorphous alloys is thought to consist mainly of Al-M and Al-Ln bondings with an attractive interaction. The equilibrium phase diagrams[19] of Al-M and Al-Ln alloys indicate the existence of a number of intermetallic compounds in

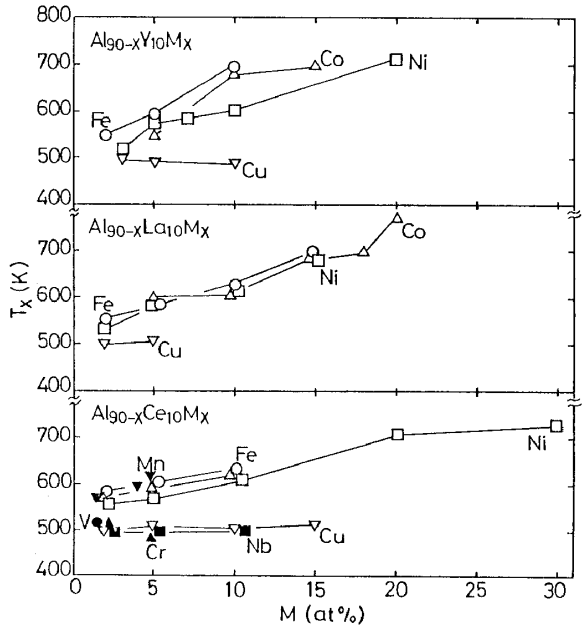

Fig. 6-14 Changes in T_x as a function of M (M=Fe, Co, Ni or Cu) concentration for $Al_{90-x}Y_{10}M_x$, $Al_{90-x}La_{10}M_x$ and $Al_{90-x}Ce_{10}M_x$ amorphous alloys.

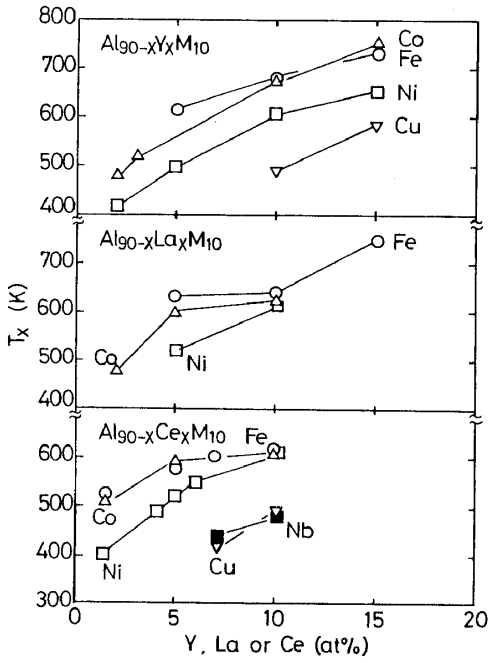

Fig. 6-15 Changes in T_x as a function of Y, La or Ce concentration for $Al_{90-x}Y_xM_{10}$, $Al_{90-x}La_xM_{10}$ and $Al_{90-x}Ce_xM_{10}$ (M=Fe, Co, Ni or Cu) amorphous alloys.

their binary alloy systems. When the formation tendency and T_m of intermetallic compounds in Al-rich composition ranges corresponding to the glass-formation ranges in the Al-Ln-M systems are compared in Al-Ln alloys, one can notice that the minimum solute concentration for the formation of Al-rich compounds is 25 %Y (Al_3Y), 20 %La (Al_4La) and 20 %Ce (Al_4Ce) and the T_m of these compounds is considerably higher for Al_4(La or Ce) than for Al_3Y[19]. These differences suggest that the attractive interaction between Al and Ln atoms is considerably stronger for Al-La and Al-Ce atoms than for Al-Y atoms. This is probably because the T_x values are higher for Al-La-M and Al-Ce-M amorphous alloys. On the basis of a similar concept that the degree of the attractive interaction between the constituent atoms exerts a significant effect on T_x, one can explain the result that T_x decreases in the order of Al-Fe-Ln > Al-Co-Ln > Al-Ni-Ln >> Al-Cu-Ln, because the T_m of Al-rich Al_3Fe, Al_9Co_2, Al_3Ni and Al_2Ce compounds decreases in the order of Fe > Co > Ni > Cu[19]. The good coincidence between T_x of the amorphous alloys and T_m of the Al-rich intermetallic compounds appears to support the appropriateness of the concept that the attractive interaction among the constituent elements contributes significantly to the glass formation of the metal-metal type amorphous alloys.

6. Mechanical properties and corrosion resistance[55,56)]

The σ_f, E and H_v of Al-Y-Ni, Al-La-Ni and Al-Ce-Ni amorphous alloys are summarized in Table 6-3, where the data of $\varepsilon_{t,f}=\sigma_f/E$, $\varepsilon_{c,y}\simeq H_v/3E$ and $\sigma_{c,y}\simeq H_v/3$ are also shown for reference. The approximation of $\varepsilon_{c,y}\simeq H_v/3E$ is based on the fact that an amorphous alloy exhibits little work-hardening and thus the compressive yield strength is related by $\sigma_{c,y}\simeq H_v/3$[27)]. As seen in the table, σ_f lies in the rage of 730 to 1140 MPa for the Al-Y-Ni alloys, 670 to 1080 MPa for the Al-La-Ni alloys, and 810 to 935 MPa for the Al-Ce-Ni alloys and is considerably higher for the Al-Y-Ni and Al-La-Ni alloys than for the Al-Ce-Ni alloys. No distinct compositional dependence of σ_f is seen for the three alloy systems, while the E, H_v and $\sigma_{c,y}$ increase with decreasing Al content from 52.4 to 84.2 GPa, 300 to 380 and 980 to 1240 MPa, respectively, for the Al-Y-Ni alloys, from 64.7 to 88.9 GPa, 260 to 320 and 850 to 1080 MPa, respectively, for the Al-La-Ni alloys, and from 53.2 to 60.3 GPa, 215 to 335 and 555 to 935 MPa, respectively, for the Al-Ce-Ni alloys. Thus, the properties except σ_f have a similar compositional dependence. Nonexistence of compositional dependence for σ_f is presumably because σ_f is highly sensitive against structure and smoothness of sample surface. At any event, it is notable that $Al_{87}Y_8Ni_5$ and $Al_{87}La_8Ni_5$ amorphous alloys exhibit high static strengths of 1080 to 1140 MPa for σ_f and 260 to 300 for H_v which greatly exceed the highest values of 550 MPa and 180[57)] for conventional Al-based crystalline alloys subjected to an optimum age-hardening treatment. The specific strength defined by the ratio of σ_f to density (ρ) is estimated to reach 38 for the $Al_{87}Y_8Ni_5$ alloy and 34 for the $Al_{87}La_8Ni_5$ alloy, being

Table 6-3 Mechanical properties of Al-Y-Ni, Al-La-Ni and Al-Ce-Ni amorphous alloys.

Alloy (at%)	σ_f (MPa)	E (GPa)	H_v	$\varepsilon_{t,f}=\sigma_f/E$	$\varepsilon_{c,y}\simeq 9.8H_v/3E$
$Al_{88}Y_2Ni_{10}$	920	71.0	340	0.013	0.016
$Al_{87}Y_8Ni_5$	1140	71.2	300	0.016	0.014
$Al_{87}La_8Ni_5$	1080	88.9	260	0.012	0.010
$Al_{84}La_6Ni_{10}$	1010	83.6	280	0.012	0.010
$Al_{86}Ce_4Ni_{10}$	810	54.6	300	0.015	0.018
$Al_{85}Ce_5Ni_{10}$	935	59.4	320	0.016	0.018

higher than that (33) reported for Ni-Si-B-Al amorphous wires[58] with σ_f of about 2750 MPa. However, these values for σ_f/ρ are slightly lower than those (40-56) for Fe-Si-B[59] and Co-Si-B[60] amorphous wires with high σ_f ranging from 3000 to 3900 MPa.

Figure 6-16 shows the fracture surface appearance of an $Al_{87}Y_8Ni_5$ amorphous ribbon fractured by uniaxial tensile test. The fracture surface consists of a smooth region (A) caused by shear sliding and a vein region (B) caused by final catastrophic fracture after shear sliding. Furthermore, it is seen that the fracture takes place along the shear plane declined by 45 to 55 degrees to the longitudinal tensile direction. A similar feature of the fracture surface appearance was also observed for Al-La-Ni and Al-Ce-Ni amorphous ribbons. These features in the fracture behavior are the same as those[28] reported previously for the other ductile amorphous alloys produced by liquid quenching. The similarity allows us to infer that the Al-based amorphous alloys have good ductility comparable to conventional ductile amorphous alloys.

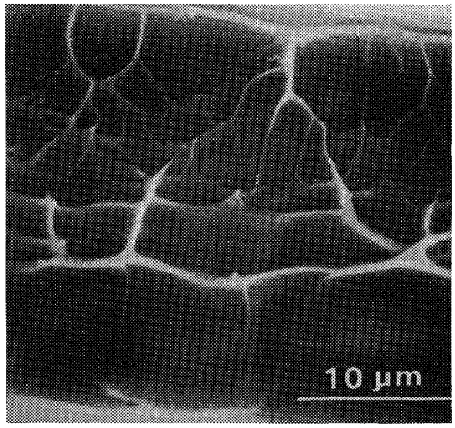

Fig. 6-16 Scanning electron micrograph showing the tensile fracture appearance of an $Al_{87}Y_8Ni_5$ amorphous ribbon.

Figure 6-17 shows the correlation between E and σ_f, H_v or T_x for Al-Y-Ni and Al-La-Ni amorphous alloys. The three properties of σ_f, H_v and T_x tend to increase with increasing E. As shown in Table 6-3 and Fig. 6-17, the correlation between E and σ_f or H_v can be empirically expressed by the following approximate equations; $\varepsilon_{t,f} = \sigma_f/E \simeq 0.015$ and $\varepsilon_{c,y} \simeq H_v/3E \simeq 0.017$. The $\varepsilon_{t,f}$ and $\varepsilon_{c,y}$ values are nearly equal to the respective values of 0.018 and 0.014[26] for the Fe-, Co-, Ni-, Pd-, Pt- and Cu-

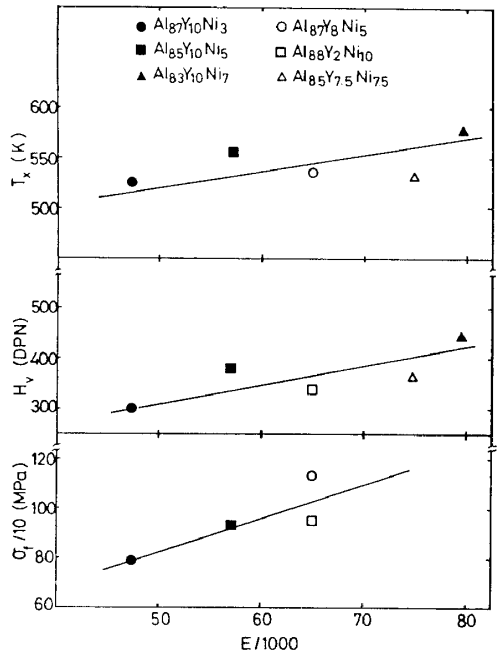

Fig. 6-17 Correlation between E and σ_f, H_v or T_x for Al-Y-Ni amorphous alloys.

based amorphous wires.

In addition, the Al-Y-Ni and Al-La-Ni amorphous alloys with high tensile strength above 1000 MPa were found to exhibit high corrosion resistance in HCl and NaOH solutions which exceed largely that of conventional Al-based crystalline alloys. As shown in Table 6-4, the corrosion losses of the Al-Y-Ni amorphous alloy in 1 N HCl and 0.25 N NaOH solutions at 293 K are 68 and 240 times, respectively, as small as those for the high-strength Al-Cu-Mg alloy subjected to an optimum heat treatment. It is particularly notable that the Al-based amorphous alloys have high corrosion resistance even in the alkalloid solution. This is in good contrast to the fact that the solution has generally been used as a reagent of Al-based crystalline alloys. The discovery of Al-Y-Ni and Al-La-Ni amorphous alloys exhibiting the high specific strength combined with good ductility and high corrosion resistance allows us to expect that the high-strength Al-based amorphous alloys will be valuable for applications in areas where their properties are required simultaneously.

Table 6-4 Corrosion losses of an $Al_{85}Y_{10}Ni_5$ amorphous alloy in 1 N HCl and 0.25 N NaOH solutions. The data of conventional Al-based crystalline alloys are also shown for comparison.

Alloy	0.25N NaOH at 293 K (mm/year)	1N HCl at 293 K (mm/year)
$Al_{85}Y_{10}Ni_5$	2.5	0.055
Al(99.99%)	18.6	0.72
Al-Cu-Mg (2024)	170.0	13.0

7. Glass transition behavior and change in fundamental properties by glass transition[61)]

Figure 6-18 shows the compositional dependences of the glass transition temperature (T_g) and T_x for amorphous Al-Y-Ni and Al-Ce-Ni alloys measured at a scanning rate of 40 K/min. In the figure, T_g is represented by an asterisk. It is seen that the glass transition phenomenon was observed prior to crystallization in the vicinity of 10 %Y for the Al-Y-Ni system and 6 %Ce for the Al-Ce-Ni system, indicating that the separation of glass transition from crystallization is mainly dominated by the Ln metals of Y and Ce and is independent of Ni content. T_g and T_x increase significantly with increasing solute concentration from 490 to 582 K and 518 to 604 K, respectively, for the Al-Y-Ni alloys and from 500 to 573 K and 517 to 600 K, respectively, for the Al-Ce-Ni alloys. In addition, Fig. 6-18 shows a general

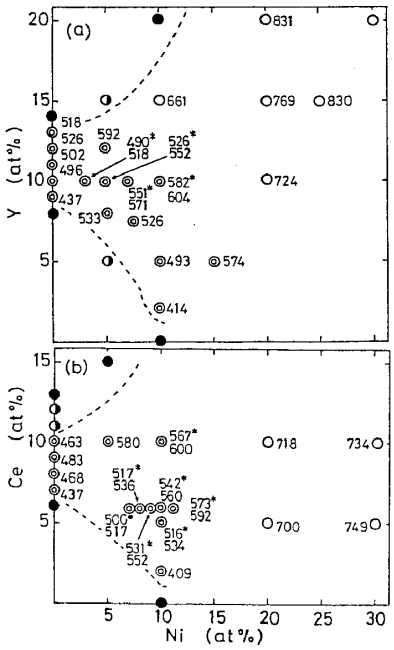

Fig. 6-18 Composition ranges for formation of amorphous phase and the changes of T_g and T_x in Al-Y-Ni (a) and Al-Ce-Ni (b) systems: (◎) amorphous (ductile); (o) amorphous (brittle); (◑) amorphous plus crystalline; (●) crystalline. The marks of asterisk represent the T_g.

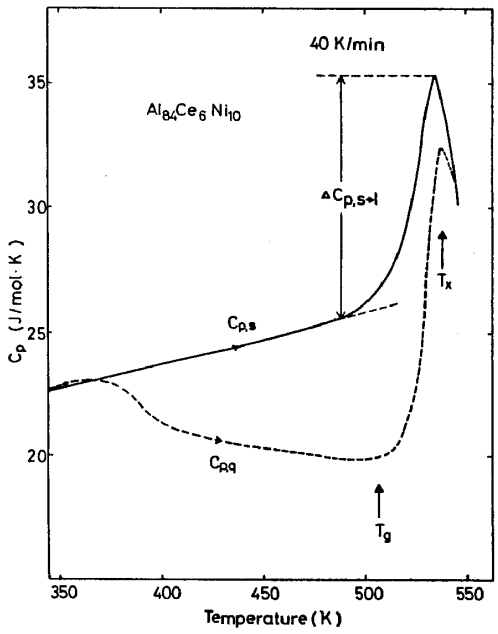

Fig. 6-19 The thermogram $C_{p,q}(T)$ of an amorphous $Al_{84}Ce_6Ni_{10}$ alloy in the as-quenched state. The solid line represents the thermogram $C_{p,s}(T)$ of the sample heated to 520 K.

tendency that the amorphous alloys exhibiting a glass transition have a good bending ductility.

As an example, Fig. 6-19 shows the thermograms of an amorphous $Al_{84}Ce_6Ni_{10}$ alloy. The C_p value of the as-quenched phase is 22.8 J/mol-K near room temperature. As the temperature rises, the C_p value increases gradually and begins to decrease, indicating an irreversible structural relaxation at about 365 K. With a further increase in temperature, the C_p value reaches its minimum at about 500 K, then increases rapidly in the region of glass transition at about 515 K and reaches 32.4 J/mol-K for the supercooled liquid around 535 K. With further increasing temperature, the supercooled liquid begins to crystallize at 540 K. Figure 6-19 also shows that their amorphous alloys have a large difference, $\Delta C_{p,s\rightarrow l}$, in specific heat between the amorphous solid and supercooled liquid reaching 9.2 J/mol-K. The difference in $C_p(T)$ between the as-quenched and the reheated states, $[\Delta C_p(T)]$, manifests the irreversible structural relaxation which is presumed to arise from the annihilation of various kinds of quenched-in "defects" and the enhancement of the topological and chemical short-range ordering through the atomic rearrangement. The T_g

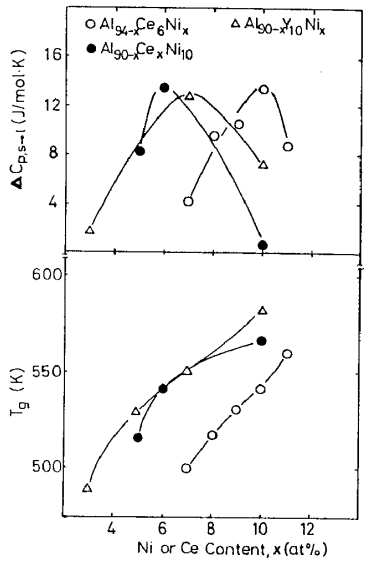

Fig. 6-20 Changes in T_g and the difference of the specific heat between amorphous solid and supercooled liquid ($\Delta C_{p,s\to l}$) as a function of Ni or Ce concentration for Al-Y-Ni, Al-La-Ni and Al-Ce-Ni amorphous alloys.

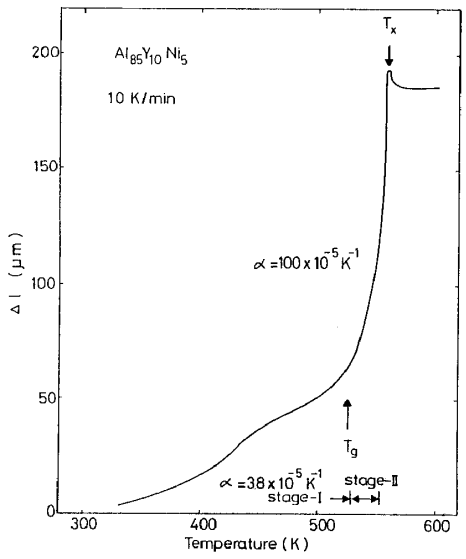

Fig. 6-21 Change in length (α) of an amorphous $Al_{85}Y_{10}Ni_5$ alloy with heating. The temperature coefficient of elongation is also shown for reference.

and $\Delta C_{p,s\to l}$ as a function of Ni or Ce concentration for the Al-Y-Ni and Al-Ce-Ni amorphous alloys are plotted in Fig. 6-20. The T_g increases almost linearly with increasing solute concentration, while the $\Delta C_{p,s\to l}$ values are the largest near the center in the compositional range where the amorphous alloys with glass transition are obtained. Considering the general tendency[62] that the larger the $\Delta C_{p,s\to l}$ value the easier is the formation of an amorphous phase, it is expected that an amorphous phase with high structural stability is obtained in the vicinity of $Al_{83}Y_{10}Ni_7$ and $Al_{84}Ce_6Ni_{10}$. Thus, the Al content of stable amorphous alloys with the largest $\Delta C_{p,s\to l}$ is nearly equal in the two alloys, but the ratios of Y or Ce to Ni are significantly different.

Figure 6-21 shows an elongation curve of an amorphous $Al_{85}Y_{10}Ni_5$ alloy measured under an initial tensile stress of 0.98 MPa at a heating rate of 10 K/min. The length of the specimen begins to increase at about 320 K and increases gradually up to about 520 K and then rapidly in the range from 530 to 560 K. With a further increase in temperature, the increase in the length stops suddenly due to crystallization. The elongation curve before crystallization can be divided into two stages corresponding to an amorphous solid and a supercooled liquid as shown in Fig. 6-21 and each temperature coefficient of elongation (α) is estimated to be 3.8×10^{-5} K^{-1} for the amorphous solid in the range of

320 to 520 K and 100×10^{-5} K^{-1} for the supercooled liquid in the range of 530 to 560 K. The extraodinarily high α value for the supercooled liquid is due to a much lower viscosity.

Based on the data shown in Fig. 6-21, the viscosities (η) as a function of temperature were evaluated for amorphous $Al_{85}Y_{10}Ni_5$ and $Al_{84}Ce_6Ni_{10}$ alloys. Figure 6-22 plotts the η values as a function of reciprocal temperature. The η values of the Al-based alloys decrease significantly from 2×10^{14} Pa.s (2×10^{15} poise) at 488 K to 3×10^{12} Pa.s at 521 K and no distinct difference in η(T) is seen for the two amorphou alloys. It is notable that the η value (3×10^{12} Pa.s) at 521 K is nearly equal to 10^{12} Pa.s which has been thought[62] to be the viscosity for a supercooled liquid near T_g, indicating that the amorphous solid heated at 521 K changes to a nearly equilibrium supercooled liquid state.

It is generally known that the glass transition gives rise to significant changes of E, σ_f and deformation behavior, in addition to the above-described changes in specific heat and viscosity. It is important for the present Al-based amorphous alloys to clarify the changes in E, σ_f, elongation and fracture behavior by the transition from amorphous solid to supercooled liquid. Figure 6-23 shows the temperature dependences of σ_f, ε_f and E for $Al_{85}Y_{10}Ni_5$ and $Al_{84}Ce_6Ni_{10}$

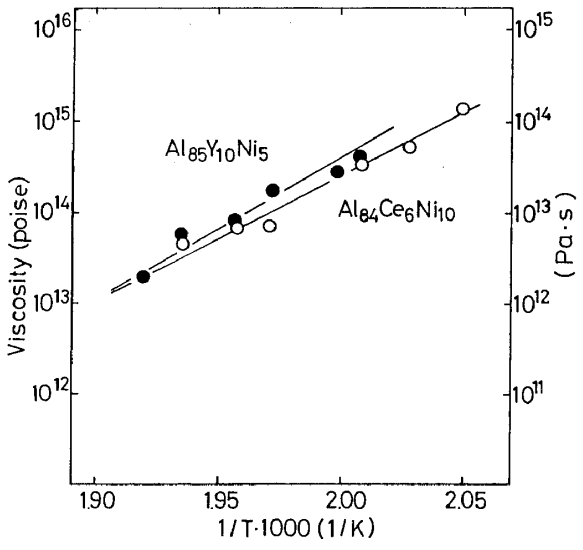

Fig. 6-22 Change in viscosity of amorphous $Al_{85}Y_{10}Ni_5$ and $Al_{84}Ce_6Ni_{10}$ alloys as a function of reciprocal temperature.

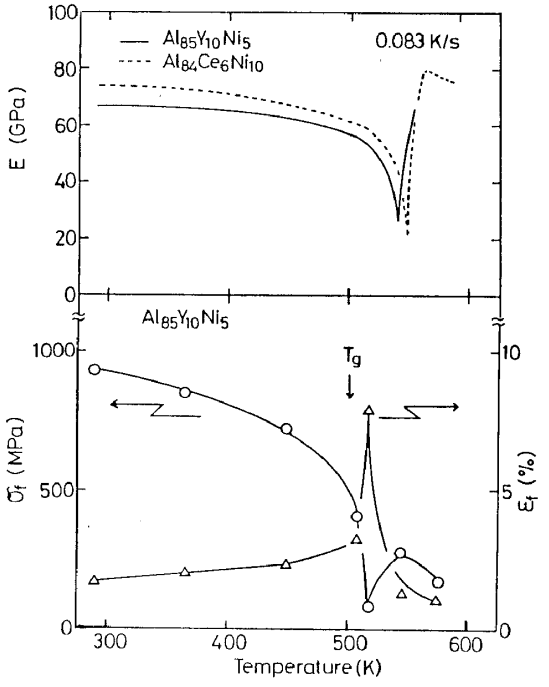

Fig. 6-23 Changes in E, σ_f and ε_f of amorphous $Al_{85}Y_{10}Ni_5$ and $Al_{84}Ce_6Ni_{10}$ alloys as a function of testing temperature.

amorphous alloys. With increasing temperature, the σ_f and E values decrease gradually from 920 to 700 MPa and 72.6 to 55.0 GPa, respectively, in the amorphous solid and rapidly to 100 MPa and 21.6 GPa, respectively, in the supercooled liquid and then increase steeply upon crystallization. On the other hand, the ε_f increases steeply to 8 % in the vicinity of glass transition, followed by a significant decrease of ε_f by crystallization. Figure 6-24 shows the fracture surface appearance of an amorphous $Al_{85}Y_{10}Ni_5$ alloy tested at 508 K near the glass transition. The specimen is subjected to a severe homogeneous necking which appears to have taken place through a viscous flow mechanism. The feature of deformation and fracture behaviors shown in Figs. 6-23 and 6-24 agrees with that[29] for Pd-based amorphous alloys exhibiting the glass transition phenomenon.

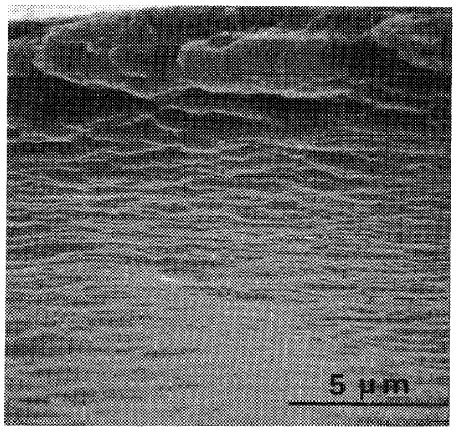

Fig. 6-24 Scanning electron micrograph showing the tensile fracture surface appearance of an amorphous $Al_{85}Y_{10}Ni_5$ alloy tested at 508 K.

8. Production of amorphous alloy powders and their consolidation into an amorphous bulk[63]

The production of Al-Ni-Y amorphous powders was tried by high-pressure helium atomization. Figure 6-25 shows the shape and morphology of an $Al_{85}Ni_5Y_{10}$ powder with a particle size fraction below 25 μm (-25 μm). The powder has a spherical shape. The surafce is very smooth and no grain boundary is seen. The X-ray diffraction pattern of the -25 μm powder consisted of broad diffraction peaks, indicating the formation of a mostly single amorphous phase. With further increasing powder diameter, the structure is composed of amorphous and crystalline phases for the 25-37 μm fraction and a

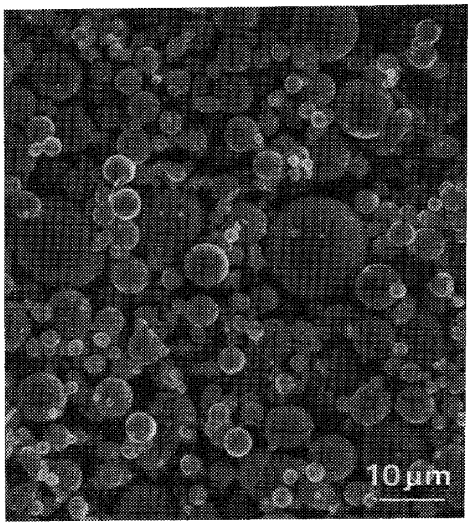

Fig. 6-25 Scanning electron micrograph showing $Al_{85}Ni_5Y_{10}$ powder with a size fraction below 25 μm produced by high-pressure helium atomization.

crystalline phase for the powder with a size fraction above 37 μm. In addition, the size fraction of the amorphous Al-Ni-Y powder was measured by the microtrac analysis method. The fraction is 41 % for the powder below 10 μm in size, followed by 24 % for the powder between 10 and 15 μm in size, 25 % for the 15 to 21 μm powder and 11 % for the powder above 21 μm in size. It is thus notable that the powder below 15 μm in size was prepared with a high yield fraction of 65 %. Furthermore, the DSC curve obtained from the $Al_{85}Ni_5Y_{10}$ amorphous powder was confirmed to be the same as that for the melt-spun amorphous ribbon and no appreciable difference in T_g and T_x values was seen[64]. It is therefore concluded that the amorphous powder produced by high-pressure helium atomization is used as a raw material to produce an amorphous bulk by consolidation at temperatures near T_g.

The extrusion of the $Al_{85}Ni_5Y_{10}$ amorphous powder into an amorphous bulk at extrusion ratios of four and seven was tried by changing the extrusion temperature. The extruded bulk was obtained at temperatures above 543 K and the relative density was measured to be 0.969 at 543 K, 0.980 at 573 K, 0.987 at 603 K and 0.996 at 673 K. The structure of the extruded bulk consists of a mostly amorphous phase at 543 K, coexisting amorphous+Al phases at 573 K and coexisting amorphous+Al+unidentified compound at 603 K and Al+compound at 673 K.

Figure 6-26 shows the compressive stress-strain curves of $Al_{85}Ni_5Y_{10}$ bulks with high densities above 98 % extruded at 603 and 673 K, along with the data of a conventional high-strength Al-based crystalline alloy (2017). It is notable that the bulk consisting of amorphous and Al exhibits high compressive fracture strength ($\sigma_{c,f}$) reaching 1470 MPa and E of 145 GPa, though no appreciable plastic elongation is seen. The increase of the extruded temperature to 673 K gives decreases of yield (0.2 % proof) stress to 1220 MPa and E to 120 GPa and an increase of plastic elongation to 0.6 %, though the $\sigma_{c,f}$ remains unchanged. In addition to the high $\sigma_{c,f}$, the tensile fracture strength is also as high as 950 MPa for an Al-Ni-Y bulk material produced by extrusion with a ratio of seven at 623 K, as exemplified for the tensile stress-strain curve in Fig. 6-27. It is notable that

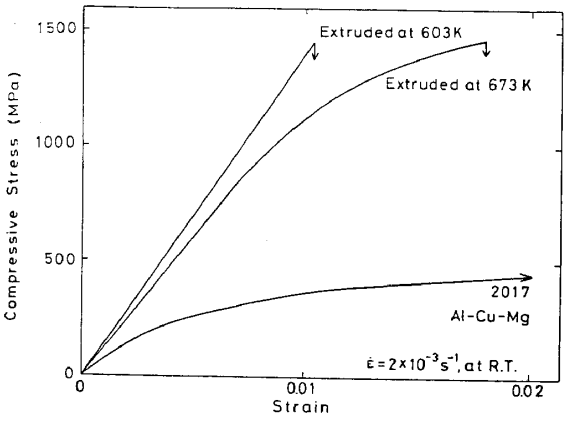

Fig. 6-26 Compressive stress-strain curves of $Al_{85}Ni_5Y_{10}$ bulks produced by extrusion of amorphous alloy powders at 603 and 673 K.

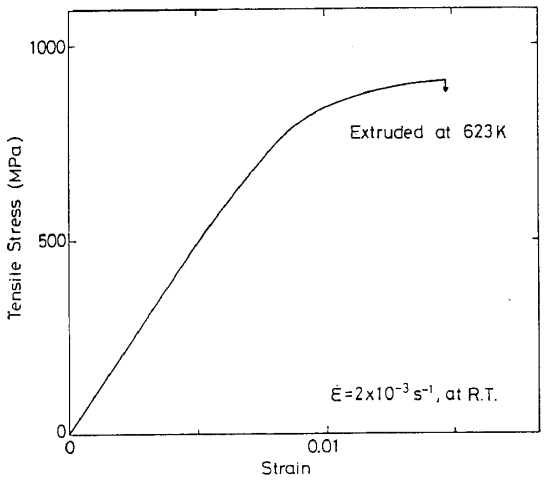

Fig. 6-27 Tensile stress-strain curve of an $Al_{85}Ni_5Y_{10}$ bulk produced by extrusion of amorphous alloy powders at 673 K and an extrusion ratio of seven.

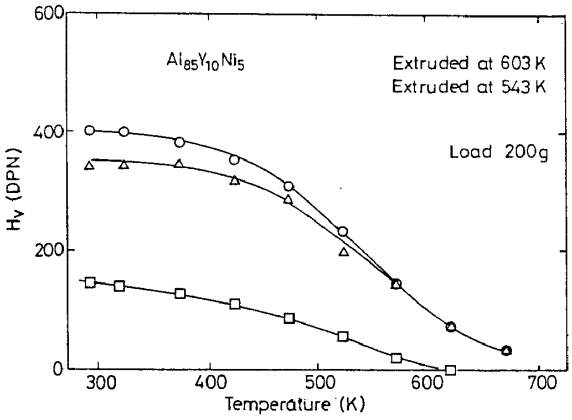

Fig. 6-28 Change in H_v of extruded $Al_{85}Ni_5Y_{10}$ bulks as a function of testing temperature.

the $\sigma_{c,f}$ and E for the bulk material with a mixed structure of amorphous and fcc phases are about 2 to 3 times as large as those (450 MPa and 71 GPa) for the optimumly aged 2017 alloy. The extremely high $\sigma_{c,f}$ which exceeds the σ_f (1140 MPa) of the $Al_{85}Ni_5Y_{10}$ amorphous ribbon is probably due to a dispersion-hardening resulting from a homogeneous dispersion of the spherical Al phase with a size of about 30 nm in an amorphous matrix. The details of the strengthening mechanism are under investigation.

The high-temerature hardness of the high-strength $Al_{85}Ni_5Y_{10}$ bulks consisting of a mostly amorphous phase or coexisting amorphous+Al phases was measured as a function of testing temperature. The heating rate to each testing temperature was 10 K/min and the sample was kept for 10 min at each testing temperature. As shown in Fig. 6-28, the H_v at room temperature is 340 for the amorphous bulk extruded at 543 K and 405 for the amorphous+Al bulk extruded at 603 K, being about three times as high as that (145) for the 2017 alloy. Furthermore, the high hardness of 150 at 573 K is obtained for the bulk extruded at 603 K. It is thus concluded that the extruded bulks have high heat-resistant hardness as well as high $\sigma_{c,f}$ and E values. The good mechanical strengths allow us to expect that the extruded bulk may be used as a high-strength material with low density under a compressive stress condition.

VII. Conclusion

All the data presented in the present review were obtained for the last two years after the discovery of ductile Al-based amorphous alloys. Accordingly, there is a high possibility of finding further improved characteristics for Al-based amorphous alloys in the near future. In any case, it is notable that the success of the amorphization of Al-based alloys with low density by the melt spinning technique gives rise to a new topic in the research field of amorphous alloys. It is hereafter hoped that the interest on the Al-based amorphous alloys increases significantly and a number of useful data, which enable us to use in various application fields, are presented by a number of researches.

References

(1) W. Klement, R.H. Wilens and P. Duwez, Nature, 187 (1960), 869.
(2) A. Inoue, M. Yamamoto, H.M. Kimura and T. Masumoto, J. Mater. Sci. Lett., 6 (1987), 194.
(3) P. Predecki, B.C. Giessen and N.J. Grant, Trans. Met. Soc. AIME, 233 (1965), 1438.
(4) P. Ramachandrarao, M. Laridjani and R.W. Cahn, Z. Metakde, 63 (1972), 43.
(5) H.A. Davies and J.B. Hull, Scripta Met., 6 (1972), 241.
(6) K. Chattopadyay, R. Ramachandrarao, S. Lele and T.R. Anantharaman, Proc. 2nd Int. Conf. Rapidly Quenched Metals, Ed. N.J. Grant and B.C. Giessen, MIT Press, Massachusetts, (1976), p.157.
(7) P. Furrer and H. Warlimont, Mater. Sci. Eng., 28 (1977), 127.
(8) G.V.S. Sastry, C. Suryanarayana, O.N. Srivastava and H.A. Davies, Trans. Indian Inst. Metals, 31 (1978), 292.
(9) A. Inoue, A. Kitamura and T. Masumoto, J. Mater. Sci., 16 (1981), 1895.
(10) A.P. Tsai, A. Inoue and T. Masumoto, Met. Trans., 19A (1988), 1369.
(11) A.P. Tsai, A. Inoue, and T. Masumoto, J. Mater. Sci. Lett., 7 (1988), 805.
(12) A. Inoue, K. Ohtera, A.P. Tsai and T. Masumoto, Jpn. J. Appl. Phys., 27 (1988), L280.
(13) A. Inoue, K. Ohtera and T. Masumoto, Jpn. J. Appl. Phys., 27 (1988), L1796.
(14) A. Inoue, K. Ohtera and T. Masumoto, Jpn. J. Appl. Phys., 27

(1988), L736.
(15) A. Inoue, K. Ohtera, T. Zhang and T. Masumoto, Jpn. J. Appl. Phys., 27 (1988), L1583.
(16) A. Inoue, T. Zhang, K. Kita and T. Masumoto, Mater. Trans., Japan Inst. Metals, 30 (1989), 870.
(17) A. Inoue, Y. Bizen, H.M. Kimura, T. Masumoto and M. Sakamoto, J. Mater. Sci., 23 (1988), 3640.
(18) H.A. Davies, Amorphous Metallic Alloys, Ed. F.E. Luborsky, Butterworths, London, (1983), p.8.
(19) Binary Alloy Phase Diagrams, Ed. T.B. Massalski, American Society for Metals, Ohio, (1986).
(20) A. Inoue, Y. Bizen, H.M. Kimura, M. Yamamoto, A.P. Tsai and T. Masumoto, J. Mater. Sci. Lett., 6 (1987), 811.
(21) J.M. Dubois, G. Le Caer and K. Dehghan, Rapidly Quenched Metals, Ed. S. Steeb and H. Warlimont, Elsevier, Amsterdam, 1985, p.197.
(22) E. Voisin and A. Pasturel, Phil. Mag. Lett., 55 (1987), 123.
(23) H.S. Chen, Rep. Prog. Phys., 43 (1980), 353.
(24) K.V. Rao, Amorphous Metallic Alloys, Ed. F.E. Luborsky, Butterworths, London, (1983), p. 401.
(25) A.P. Tsai, A. Inoue and T. Masumoto, Met. Trans., 19A (1988), 391.
(26) A. Inoue, M. Hagiwara and T. Masumoto, Sci. Rep. Res. Inst. Tohoku Univ., 34A (1988), 48.
(27) H.S. Chen, J.T. Krause and E. Coleman, J. Non-Cryst. Solids, 78 (1975), 157.
(28) T. Masumoto and R. Maddin, Acta Met., 19 (1971), 725.
(29) W.L. Johnson, Rapidly Quenched Metals III, Ed. B. Cantor, The Metals Society, London, 1978, Vol.2, p.1.
(30) A. Inoue and T. Masumoto, Sci. Rep. Res. Inst. Tohoku Univ., A-29 (1981), 305.
(31) M. Nose and T. Masumoto, Sci. Rep. Res. Inst. Tohoku Univ., A-28 (1980), 222.
(32) A. Inoue, K. Kobayashi and T. Masumoto, Metallic Glasses, Science and Technology, Ed. C. Hargitai et al., Cent. Res. Inst. Phys., Budapest, 1980, Vol.2, p.217.
(33) T. Egami and Y. Waseda, J. Non-Cryst. Solids, 64 (1984), 113.
(34) A.R. Miedema, F.R. de Boer and R. Boom, CALPHAD, Pergamon Press, Great Britain, 1977, Vol.1, No.4, p.341.
(35) E. Matsubara, Y. Waseda, A. Inoue, K. Ohtera and T. Masumoto, Z. Naturforsch., 44a (1989), 814.
(36) E. Matsubara, K. Harada, Y. Waseda and M. Iwase, Z. Naturforsch., 43a (1988), 181.
(37) H.F. Buhner and S. Steeb, Z. Naturforsch., 24a (1969), 428.

(38) S. Steeb and R. Hezel, Z. Metallkde, 57 (1963), 374.
(39) H.S. Chen, D. Koskenmaki and C.H. Chen, Phys. Rev. B, 35 (1987), 3715.
(40) E. Matsubara, K. Harada, Y. Waseda, H.S. Chen, A. Inoue and T. Masumoto, J. Mater. Sci., 23 (1988), 753.
(41) Y. Waseda, Structure of Non-Crystalline Materials, McGraw-Hill, New York, 1980, p.60.
(42) C. Kittel, Introduction to Solid State Physics 5th Ed., John Wiley & Sons, Inc., New York, 1976, p.32.
(43) M. Pont, J. Gonzalo, K.V. Rao and A. Inoue, Phys. Rev. B, 40 (1989), 1345.
(44) E. Matsubara, K. Harada, Y. Waseda, A. Inoue, Y. Bizen and T. Masumoto, J. Mater. Sci., 23 (1988), 3485.
(45) R. Delgado, H. Armbruster, D.B. Naugle, C.L. Tsai, W.L. Johnson and A. Williams, Phys. Rev. B, 34 (1986), 8288.
(46) G. Bush and H.J. Guntherrodt, Solid State Physics, Ed. F. Seitz and D. Turnbull, Academic, New York, 1974, Vol.29, p.235.
(47) P. Steiner, H. Hochst, W. Steffen and S. Hufner, Z. Phys. B, 38 (1980), 191.
(48) P.J. Cote and L.V. Meisel, Glassy Metals I, Ed. H.J. Guntherodt and H. Beck, Topics in Applied Physics, Vol.46, Springer-Verlag, Berlin, 1981.
(49) A. Inoue, A.P. Tsai, K. Ohtera, K. Matsuzaki and T. Masumoto, Proc. MRS Int. Meeting on Advanced Materials, Vol.3, Ed. M. Doyama et al., MRS, Pittsburgh, 1989, p.411.
(50) B.L. Blackford, J. Low Temp. Phys., 23 (1976), 43.
(51) M.M. Collver and R.H. Hammond, Phys. Rev. Lett., 30 (1973), 92.
(52) T.R. Orlando, E.J. McNiff. Jr., S. Foner and M.R. Beasley, Phys. Rev. B, 19 (1979), 4545.
(53) U. Mizutani, T. Hasegawa, K. Fukamichi, T. Goto and T. Matsuda, Mater. Trans., Japan Inst. Metals, 30 (1989), 951.
(54) W.L. McMillan, Phys. Rev., 167 (1968), 331.
(55) A. Inoue, K. Ohtera, A.P. Tsai and T. Masumoto, Jpn. J. Appl. Phys., 27 (1988), L479.
(56) A. Inoue, K. Ohtera, A.P. Tsai and T. Masumoto, Proc. MRS Int. Meeting on Advanced Materials, Vol.3, Ed. M. Doyama et al., MRS, Pittsburgh, 1989, p.251.
(57) Metals Databook, Ed. Japan Inst. Metals, Maruzen, Tokyo, 1983, p.175.
(58) A. Inoue, S. Furukawa, M. Hagiwara and T. Masumoto, Met. Trans., 18A (1987), 621.
(59) M. Hagiwara, A. Inoue and T. Masumoto, Met. Trans., 13A (1982),

373.
(60) M. Hagiwara, A. Inoue and T. Masumoto, Mater. Sci. Eng., 54 (1982), 197.
(61) A. Inoue, K. Ohtera, A.P. Tsai, H.M. Kimura and T. Masumoto, Jpn. J. Appl. Phys., 27 (1988), L1579.
(62) H.S. Chen, Glass: Science and Technology, Vol.3, Academic Press Inc., New York, 1986, p.181.
(63) A. Inoue, K. Ohtera, K. Kita and T. Masumoto, Proc. The First Japan Int. SAMPE Symposium and Exhibition, Ed. N. Igata et al., Nikkan Kogyo Shimbun Ltd., Tokyo, 1989, p. 7.
(64) A. Inoue, K. Kita, K. Ohtera and T. Masumoto, J. Mater. Sci. Lett., 7 (1988), 1287.